Composite Structures 312 (2023) 116859

Contents lists available at ScienceDirect

Composite Structures

journal homepage: www.elsevier.com/locate/compstruct

Cracking behaviour of textile-reinforced concrete with varying concrete cover and textile surface finish

Philipp Preinstorfer [a,b,*], Serdar Yanik [c], Johannes Kirnbauer [c], Janet M. Lees [a], Agathe Robisson [c]

[a] Department of Engineering, University of Cambridge, 7a JJ Thomson Ave, Cambridge CB3 0FA, United Kingdom
[b] Institute of Structural Engineering, TU Wien, Karlsplatz 13/212-2, 1040 Vienna, Austria
[c] Institute of Material Technology, Building Physics and Building Ecology, TU Wien, Karlsplatz 13/207-1, 1040 Vienna, Austria

ARTICLE INFO

Keywords:
Textile reinforcement
Textile-reinforced concrete
TRC
Cracking behaviour
Splitting cracks
Longitudinal cracking

ABSTRACT

The cracking behaviour of textile-reinforced concrete (TRC) impacts the serviceability and structural integrity of TRC beams. However, textile reinforcement has not yet been standardised and there are numerous available textile reinforcement options. In spite of evidence that the textile properties influence the cracking behaviour of TRC, knowledge of the role of the textile, concrete and geometric parameters on cracking is still limited. This paper investigates a commonly used subset of textile reinforcements, namely epoxy-impregnated textiles with a high yarn count, some of which are prone to induce splitting failure. Through a comprehensive experimental study of 144 uniaxial reinforced concrete tensile tests, the influence of the textile fibre strand geometry and surface finish (plain or sand-coated) on the cracking behaviour was investigated in dependency of the concrete cover thickness. The results show that sand-coating treatment can decrease the transverse crack width to one-third of those observed in analogous plain textile specimens. The geometry of the plain fibre strands, which is affected by the textile fabrication method, also leads to significant differences in the measured crack widths (factor of 2.5). The overall cracking behaviour, however, is decisively influenced by the occurrence of splitting (longitudinal) cracks in the layer of the textile reinforcement, which were observed regardless of the surface treatment for concrete covers thicker than 15 mm. In case of the sand-coated textiles, these splitting cracks initiated immediately after the first main crack and propagated throughout the specimen, which diminished any tension stiffening effect. In the plain textile samples, the cracks led to an excessive spalling of the concrete cover. The results of this study provide a deeper understanding of the cracking behaviour of TRC with epoxy-impregnated textiles and a comprehensive database for further research. This establishes the basis for unified regulations regarding the limit states of TRC structures.

1. Introduction

Textile reinforcement is a fundamentally new type of reinforcement for concrete. This reinforcement is made of a multitude of continuous high-performance fibres (filaments) that are bundled into yarns. Using highly automatised textile fabrication methods, these yarns are processed to form a two-dimensional plane-like reinforcement mesh. Textile reinforcement is characterised by superior mechanical properties; for example, the tensile strength of carbon textile reinforcement (>4 GPa) can be up to eight times higher than the tensile strength of steel reinforcement [1]. Most importantly, carbon textile reinforcement is highly resistant to corrosion [2], the main cause of damage in steel-reinforced concrete (RC) structures [3]. These properties make textile-reinforced concrete (TRC) a promising solution to reduce material consumption in the concrete industry and foster more sustainable developments in this sector [4,5].

Textile reinforcement can be used for rehabilitation (often referred to as textile-reinforced mortar or TRM [6,7]) and for new construction (textile-reinforced concrete or TRC [8,9]). For newly built structures, there is a trend towards the use of epoxy-impregnated yarns with a larger fibre cross-sectional area [10,11] (subsequently referred to as fibre strands in this paper), thus providing higher tensile resistance and being more cost-competitive [12]. While numerous investigations into the bearing capacity of structures reinforced with such textile

* Corresponding author.
E-mail address: philipp.preinstorfer@tuwien.ac.at (P. Preinstorfer).

https://doi.org/10.1016/j.compstruct.2023.116859
Received 30 September 2022; Received in revised form 21 December 2022; Accepted 25 February 2023
Available online 2 March 2023

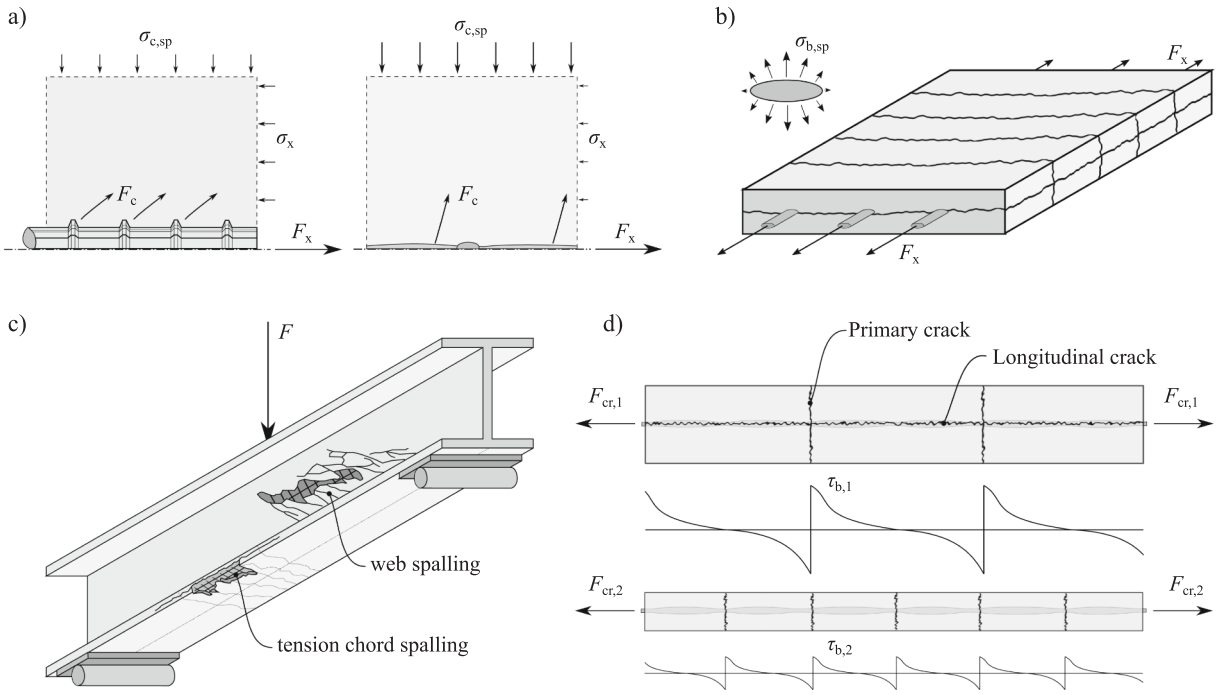

Fig. 1. Mechanical interlock that is enabled by repeating variations in the textile cross-sectional dimensions (a), longitudinal cracking in the layer of the textile reinforcement due to the elliptical shape of fibre strands (b), observed spalling that affects the structural behaviour (c) and influence of concrete cover on the splitting behaviour ($t_2 < t_1$ resulting in $F_{cr,2} < F_{cr,1}$) (d).

reinforcement have been conducted in recent years [13–16], there is still a lack of knowledge on the serviceability limit state. Understanding the cracking behaviour of TRC is of great importance in this context. Despite growing evidence that the geometric and mechanical properties of textiles impact the cracking behaviour of the reinforced concrete [17], the reinforcements have not yet been standardised, nor have minimum requirements for their respective properties been defined. The wide variation in fibres, impregnation materials (also referred to as the matrix) and textile fabrication methods, coupled with a lack of studies clarifying the important parameters that influence the reinforced concrete behaviour, means that selecting the most suitable textile reinforcement for a given application is challenging.

The cracking behaviour of reinforced elements is determined by the reinforcement bond performance and the concrete tensile properties. In recent studies, for example, it was shown that epoxy-impregnated fibre strands which exhibit a repeating variation in cross-sectional dimensions enable a mechanical interlock between the fibre strand and the concrete (see Fig. 1a) similar to the effect in steel reinforced concrete, thus providing a high bond strength and stiffness [18,19]. This usually results in narrow crack distances and small crack widths. In the case of strong bonding, however, high splitting tensile stresses occur in the concrete [19], raising concerns that textile reinforcement which promotes interlocking tends to cause splitting cracks in the concrete [13,20]. This may even be accompanied by an excessive spalling of the concrete cover and a significant drop in the bond performance once the splitting crack occurs, as was observed in recent studies, particularly on fibre strands with an elliptical cross-sectional geometry [15,21] (see Fig. 1b and c). To avoid splitting cracks in steel reinforced concrete, the concrete cover is usually increased. In the case of TRC, however, a contradictory behaviour is theoretically predicted, as the geometry of the fibre strands impacts the distribution of the splitting tensile stresses [20,22], with the splitting stresses due to bond action $\sigma_{b,sp}$ being mainly orientated perpendicular to the reinforcement layer in the case of fibre strands with the aforementioned elliptical cross-sectional shape (see Fig. 1b). And while the cracking load F_{cr} and thus the crack distance increases with increasing cover thickness, leading to higher bond stresses τ_b and hence higher splitting tensile stresses $\sigma_{c,sp}$, the splitting resistance in the textile layer does not increase (see Fig. 1d). This behaviour underlines a complex correlation between the cracking behaviour and the geometrical parameters of the reinforcement and the concrete cover thickness, making it difficult to predict the actual cracking behaviour of TRC [23]. Additional measures to improve the bond performance of textile reinforcement, like sand-coating [10,24], make the prediction of the cracking behaviour even more challenging.

In this manuscript, we aim to shed light on the cracking behaviour of epoxy-impregnated heavy tow fibre strands (>2400 tex) embedded in a cementitious matrix. For this purpose, a total of 144 TRC samples were tested under uniaxial tension, where the concrete cover thickness and the surface finish of the textiles (plain or sand-coated) were varied. Because different types of textiles are part of this study, the geometric properties of the fibre strands such as the cross-sectional geometry and repeating variation in cross-sectional dimension along the fibre strand length were of interest. These properties were therefore determined precisely using a laser scanner [25,26] so that also their influence on the cracking behaviour could be captured. Digital image correlation (DIC) image acquisition and analysis methods to continuously track the onset and progression of cracks during the uniaxial tension tests, on the front and side of all the specimens, were also invoked. Data post-processing using a Matlab-script enabled an automated evaluation of crack width and distance. By comparing the different textile reinforcements, we could identify the critical parameters controlling the cracking behaviour and qualitatively display their influence on the crack distances and crack widths in TRC. This study thus enables a sound understanding of the cracking behaviour of epoxy-impregnated heavy-tow textile reinforcement embedded in a cementitious matrix and provides a comprehensive database for future research in this field.

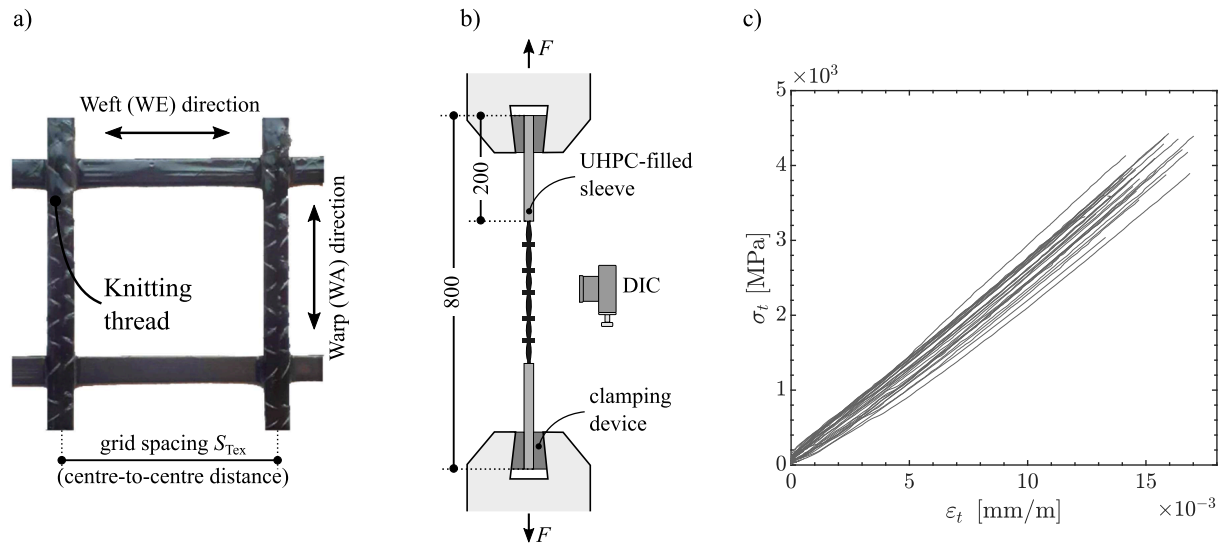

Fig. 2. Textile reinforcement with fibre strands in weft and warp direction (a), test setup for testing the material properties of the textile reinforcement (unit: mm) (b) and stress–strain response of the fibre strands under uniaxial tension (c).

Table 1
Properties of textile reinforcements. A_{Tex} (textile fibre cross-section areas per meter length) and S_{Tex} (grid spacing) were given by the supplier. A_f (cross-sectional area of fiber strand), U_f (circumference), $f_{t,f}$ (fibre strand strength), $\varepsilon_{t,f}$ (strain at failure) and E_f (Young's modulus) were measured and are listed as mean value (μ) or mean value and standard deviation (μ ± σ). S, P refers to surface finish (Sand-coated or Plain), while WE and WA refers to fibre strand fabrication direction (Weft or Warp).

	A_{Tex} [mm²/m]	S_{Tex} [mm]	Surface finish	Direction	A_f [cm²]	U_f [mm]	$f_{t,f}$ [MPa]	$\varepsilon_{t,f}$ [%]	E_f [GPa]
GRID Q85/85–21	85	21	S	WE	0.0694	11.44	4262 ± 261	15.7 ± 0.94	265 ± 6
			P	WE	0.0403	8.68	4158 ± 357	15.45 ± 0.75	263.4 ± 10.5
GRID Q95/95–38	95	38	S	WA	0.1155	13.19	3883 ± 328	14.22 ± 0.28	266.7 ± 16.6
				WE	0.1354	14.59	3997 ± 180	15.16 ± 0.41	262.1 ± 21.8
			P	WA	0.0843	11.13	4094 ± 421	15.79 ± 1.93	255.8 ± 5.1
				WE	0.0866	12.74	3813 ± 419	15.46 ± 1.63	248.9 ± 13
GRID Q142/142–38	142	38	S	WA	0.1227	14.42	3801 ± 149	14.8 ± 1.89	251.9 ± 13.8
				WE	0.1397	16.94	3922 ± 261	15.2 ± 1.44	252.1 ± 12.1
			P	WA	0.1391	14.84	3552 ± 200	13.29 ± 1.34	260.2 ± 19
				WE	0.1380	13.86	3738 ± 305	14.25 ± 1.57	259.6 ± 4.6

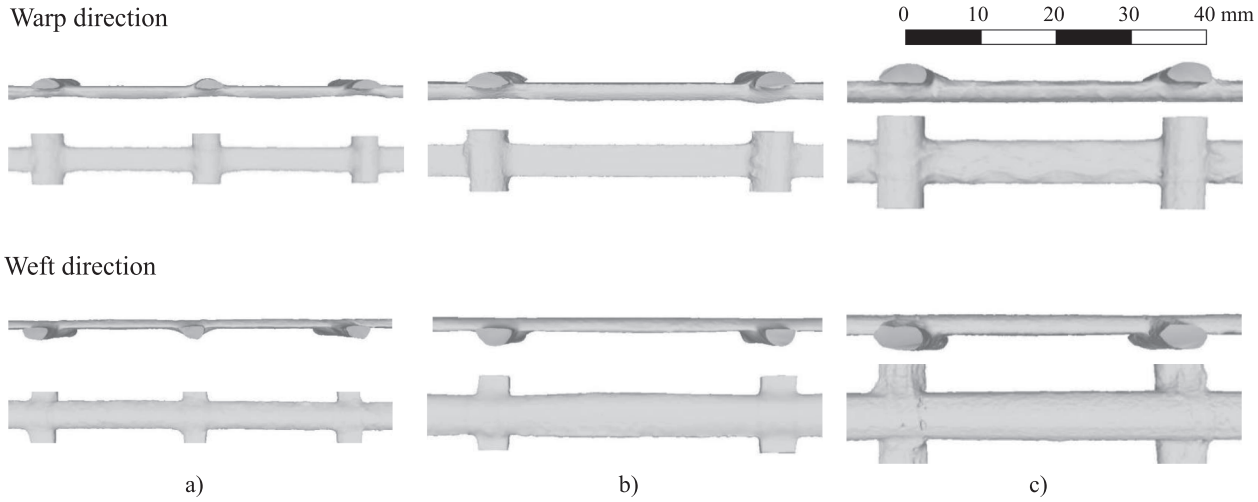

Fig. 3. Side view (top) and plan view (bottom) in warp and weft directions for the textile reinforcement, derived from a 3D model that was generated from the laser scans: Q85/85–21 (a), Q95/95–38 (b) and Q142/142–38 (c).

Table 2
Mix design of concrete.

CEM I 42.5R [kg/m^3]	Microsilica [kg/m^3]	Limestone Powder [kg/m^3]	Sand 0/1 mm [kg/m^3]	Water [kg/m^3]	Superplasticizer [kg/m^3]
569.16	62.61	113.83	1419.08	164.1	22.77

Table 3
Properties of all concrete batches mixed to cast the samples in a given series. Each result is the mean value measured on three samples casted from the same batch. Testing was done at least 28 days after casting, and at a similar time than the composites.

Specimen	$f_{c,100cube}$ [MPa]	f_{ct} [MPa]	E_{ct} [GPa]
	batch 1/batch 2	batch 1/batch 2	batch 1/batch 2
Q85-S	133.68/[1]	–[1]	–[1]
Q85-P	119.31/[1]	7.84/6.65	38.07/39.22
Q95-S	124.06/124.97	7.24/7.94	36.75/48.45
Q95-P	149.50/141.17	8.29/7.03	39.44/40.61
Q142-S	116.55/132.69	7.06/6.51	35.69/38.23
Q142-P	124.34/123.67	9.13/8.37	37.15/39.80
$\mu \pm \sigma$	128.64 (±10.2)	7.56 (±0.8)	39.21 (±3.5)

[1] not measured S…Sand coated; P… Plain.

2. Materials and methods

2.1. Materials

2.1.1. Textile reinforcement

Six different types of epoxy impregnated carbon textile reinforcement were sourced from the company SOLIDIAN. The products were all categorised as heavy tow (>2400 tex) textiles. Three geometries were studied, with textile cross-sectional areas per meter length A_{Tex} of 85, 95 and 142 mm^2/m, and grid spacings S_{Tex} of 21 and 38 mm, respectively (see Fig. 2a and Table 1). For each geometry, the textile was procured without (plain, P) and with sand-coating (S). The mechanical properties of the fibre strands in each direction (weft and warp) were measured using strands with a specific length of 80 cm, embedded on both ends in an ultra-high performance concrete (UHPC) filled sleeve (see Fig. 2b). An anchorage length of 20 cm was chosen to avoid failure due to clamping. For each type of textile, three samples per direction were tested (weft and warp) at an axial displacement velocity of 1 mm/min. The displacements were measured using 2D image correlation. The fibre strand stress $f_{t,f}$ and the strain at failure $\varepsilon_{t,f}$ were derived from the maximum load and displacement. The Young's modulus E_f was determined using a linear fit between 0.1 and 0.9 $f_{t,f}$. The measured reinforcement properties are listed in Table 1. The mechanical response of all the fibre strands was linear elastic until a brittle rupture led to failure (see Fig. 2c).

In addition to determining the mechanical properties, the geometric properties were determined by scanning the textiles with a Metris MMD50 laser scanner that was attached to a Nikon/Metris 3600 articulated arm, with an accuracy of 7 μm. With the 3D model that is generated from the laser scans, the cross-sectional area A_f and the circumference U_f of the fibre strands (gross values including fibres and matrix) can be determined with a high precision [23] using a mean value along the length of the scans (determined volume and surface area respectively, divided by the length) that also accounts for geometric deviations of the fibre strand (e.g. at the intersection with the transverse fibre strand). The measured values are listed in Table 1. In case of GRID Q142/142–38, the circumference and cross-sectional area of the plain textile is larger than these of the sand-coated one. This is attributed to the different batches and underlines the potentially large scatter in the geometry of textiles.

The 3D models of the laser scans are depicted in Fig. 3. For textile types Q95/95–38 and Q142/142–38, it is apparent that neither of these fibre strands exhibits a pronounced regularly repeating variation in cross-sectional dimensions even though regular patterns have been previously observed for earlier generations of this type of textile [13,18,19]. However, Q142/142–38 was knitted using a tricot binding with a needle offset, which creates a rough surface on the warp thread. This ribbed surface is not present in the case of the warp fibre strand of type Q95/95–38, which was knitted using double-tricot binding. The same binding type was used for Q85/85–21, where a slight repeating variation in cross-sectional dimension was observed.

The resin content appeared to be quite high, leading to a smooth surface of the fibre strands. While the exact value of the resin content is commercially sensitive, it was noticeable that the connections to the transverse fibre strands were rather stiff, whereas in previous generations of these textiles, e.g. as studied in [25], the transverse fibre strands could be easily detached by hand.

2.1.2. Concrete

All specimens were made using a high-performance concrete (HPC) with a maximum aggregate size of 1 mm. The mix design for one cubic meter of concrete is listed in Table 2. Additionally, small portions of shrinkage compensator (5.6 kg/m^3) and defoamer (1 kg/m^3) were added.

Due to the 50-litre capacity of the concrete mixer, twelve concrete mixes were prepared following the same recipe to cast all the TRC specimens. For each series, concrete samples were cast to determine the material properties of the concrete: 100 × 100 × 100 mm^3 cubes to measure compressive strength $f_{c,100,cube}$ and 40 × 40 × 160 mm^3 prisms to measure the tensile Young's modulus E_{ct} (un-notched) and the uniaxial tensile strength f_{ct} (notched). The samples were demoulded after one day and put into a water bath kept at 22 °C for 14 days. The specimens were then stored in an ambient environment at 22 °C. All tests were performed at least 28 days after casting. The notation in Table 3 for the specimen series refers to the fabric type (value of A_T) Q85, Q95 or Q142, followed by the surface treatment (plain P or sand coated S). The last line of the table shows the average value μ and standard deviation σ across all the concrete batches. These values were used in the calculation of the strain at crack onset in the analysis of the TRC samples.

2.2. TRC samples and test setup

The concrete cover thickness was also varied to ascertain the relationship between textile geometry, surface finish and cover. The cover was increased from 5 to 30 mm with an interval of 5 mm, with the textile being placed in the middle of the sample (see Fig. 4a). The thickness of the specimen is then two times the concrete cover plus the thickness of the textile reinforcement t_{tex}, which was taken to be 5 mm in all cases. The overall specimen size was 120 × 800 mm^2 (width × length), which is consistent with examples from the literature [27–29] that used textile cuts of similar dimensions and symmetry of the reinforcement. Spacers were used to hold the textile in the middle of the formwork, and the casting was done with the formwork for the panels in an upright position. A total of 144 TRC specimens were cast using 12 concrete batches (see Table 3) with the mix design specified in Table 2. The specimen treatment was the same as for the material testing samples (demoulded after one day, put into a water bath kept at 22 °C for 14 days and then stored in an ambient environment at 22 °C until testing).

The test setup for the TRC samples can be seen in Fig. 4. A Wolpert universal hydraulic test machine was used. The clamping mechanism was designed and fabricated for this study, with a grip of 120 × 120 mm to provide the necessary anchorage length for the textiles. Sandpaper was also glued onto the gripping plates to minimise slippage. To distribute the clamping force as evenly as possible, wooden plates were placed between the steel plates and the specimen. The clamping force C was controlled using a torque wrench and ranged from 50 kN for specimens with reinforcement type Q85 and Q95 to 75 kN for type Q142,

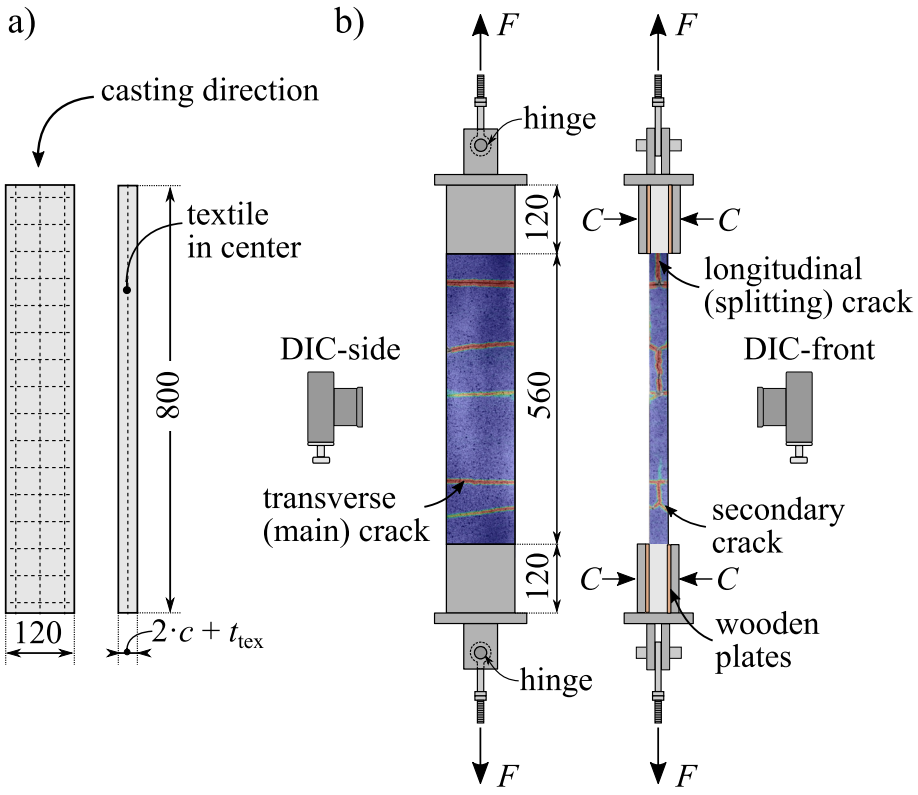

Fig. 4. Test specimen dimensions (c is the concrete cover thickness and t_{tex} the textile thickness) (a)and uniaxial tensile test set up including two video cameras to record the front and side of the sample (b).

since in that case a higher failure load was expected [30]. Finally, a fisheye ball bearing was used for alignment on both ends of the grips.

Two video cameras were used simultaneously on two faces (front and side) of the specimens to track the crack formation and crack width evolution during the experiments. The video files were synchronised and analysed using a digital image correlation (DIC) software, GOM Correlate 2019 [31]. To create contrast on the surfaces, the faces of the specimen were first painted white and then sprayed with black paint to obtain a random pattern. To keep the video file size manageable (4 K), the video frame rate was reduced to 1 frame per second (fps). The analysis was performed with a set of assigned facets (17 × 17 pixels) suitable for the size of the recorded random pattern, given the distance between the video recorder and the specimen. The resolution of the images and the DIC analysis is 31.5 μm, enabling the detection of cracks invisible to the human eye.

To perform a test, a sample was fixed in the universal testing machine and pulled in tension until a 1000 N force was reached. The sample was then tested with an imposed velocity of 1 mm/min until rupture of the textile. To estimate the variability, three repeat specimens with the same textile in the weft direction were tested. In the warp direction, only one sample was tested for comparison with the weft direction.

2.3. Data curation and progression

The specimen notation used in the following sections begins with the concrete cover thickness (5 – 30 mm), followed by the cross-sectional area of the textile per meter (85, 95 and 142) and the direction of testing (WE – weft and WA – warp). The last letter defines the surface finish (S – sand coating and P – Plain). The fibre cross-sectional area per fibre strand $A_{tex,i}$ and the number of fibre strands n per specimen are listed in Table 4. Specimens reinforced with Q85/85–21 and Q95/95–38 had the same reinforcement area per specimen (10.86 mm^2), because in the latter only three fibre strands instead of six were present in the specimens. This leads to a reinforcement ratio ρ in the range of 0.14 to 0.62% depending on the sample cover thickness. There were also three fibre strands present in the specimens reinforced with textile type Q142/142–38, but due to the larger fibre-cross sectional area, the reinforcement ratio increases and ranges from 0.21 to 0.92%.

Furthermore, the mean values of the applied load at first cracking F_{cr} and the ultimate load $F_{t,u}$ are listed in Table 4. Note that with increasing concrete cover thickness, the cracking load increases. The ultimate tensile stress $f_{t,u}$ ($F_{t,u}$ divided by fibre strands cross-sectional area in the specimens $A_{Tex,n}$; see Table 4) should be closely related to the textile tensile strength f_t and the ratio $f_{t,u}$ / f_t was used to assess the reliability of the test result. A ratio close to 1 shows that sufficient anchorage was achieved. Slightly lower ratios are attributable to the fact that increasing the number of fibre strands (brittle behaviour) leads to a statistically decreased tensile strength [32]. A ratio much lower than 1 is indicative of an anchorage failure and the data is treated accordingly (as will be described in subsequent sections). The last column of Table 4 presents information about the failure modes which will be defined later in the paper. An asterisk marks data which were excluded from the datasets due to asymmetric loading that occurred if the reinforcement deviated from the centre plane of the specimens during casting, or due to excessive slippage of the specimen during testing.

In the following steps, the raw data stemming from the digital image correlation (DIC) measurements were further processed and analysed. DIC enables the calculation of a displacement field based on speckle images, which are then processed to calculate principal strains. It can be used for continuous crack detection in reinforced concrete with a high resolution [33,34]. A crack was defined when the maximal principal strain reached the concrete failure strain (defined as tensile strength f_{ct} divided by Young's modulus E_{ct}), computed for the specific concrete batch. After a crack appeared, the crack opening was continuously monitored. The obtained datasets were synchronised by timestamps with the load monitored by the testing machine. The analysis procedure for each specimen is shown in Fig. 5. To evaluate the stress–strain behaviour, a section was created in the middle of the front surface of the

Table 4
Tensile test results (average values): cracking load of first transverse crack F_{cr}, failure load of the specimen $F_{t,u}$, tensile stress in the textile at failure $f_{t,u}$ and ratio of $f_{t,u}$ / f_t. $A_{tex,i}$ is the fibre cross-sectional area of one fibre strand, while n is the number of fibre strands in the specimen, the total fibre-cross sectional area per specimen is $A_{tex,n}$. The last column describes the failure mode of each specimen according to the definitions in Fig. 6.

Specimen	$A_{tex,i}$ [mm^2]	n [-]	$A_{tex,n}$ [mm^2]	ρ [%]	F_{cr} [kN]	$F_{t,u}$ [kN]	$f_{t,u}$ [MPa]	$f_{t,u}$ / f_t [-]	Failure mode
5–85-WE-S	1.81	6	10.86	0.62	5.86	44.01	4052.85	0.95	(a)*, (a), (a), (a)
10–85-WE-S				0.37	9.85	44.76	4121.21	0.97	(a)*, (a), (a), (a)
15–85-WE-S				0.26	13.34	46.05	4240.09	0.99	(c)*, (c), (c)*, (c)
20–85-WE-S				0.20	19.39	37.46	3449.55	0.81	(c), (c)*, (c), (c)*
25–85-WE-S				0.17	18.76	44.01	4052.50	0.95	(c), (c)*, (c)*, (c)
30–85-WE-S				0.14	28.70	44.97	4140.84	0.97	(c), (c)*, (c), (c)
5–95-WA-S	3.62	3	10.86	0.62	3.85	34.92	3215.29	0.83	(b)*
10–95-WA-S				0.37	10.75	26.77	2464.83	0.63	(b)
15–95-WA-S				0.26	20.43	42.39	3903.50	1.01	(c)
20–95-WA-S				0.20	30.03	39.29	3617.59	0.93	(c)
25–95-WA-S				0.17	21.46	43.22	3979.79	1.02	(c)
30–95-WA-S				0.14	17.93	43.43	3998.62	1.03	(c)
5–95-WE-S	3.62	3	10.86	0.62	5.59	43.00	3959.35	0.99	(a), (a), (a)
10–95-WE-S				0.37	8.82	43.64	4018.34	1.01	(a), (b)*, (a)
15–95-WE-S				0.26	23.17	43.86	4038.54	1.01	(c), (c), (c)
20–95-WE-S				0.20	27.62	42.20	3885.91	0.97	(c), (c), (c)
25–95-WE-S				0.17	28.48	41.23	3796.36	0.95	(c), (c), (c)
30–95-WE-S				0.14	27.96	42.06	3873.33	0.97	(c)*, (c)*, (c)*
5–142-WA-S	5.42	3	16.26	0.92	6.10	45.32	2787.39	0.73	(b)*
10–142-WA-S				0.55	7.18	61.05	3754.61	0.99	(a)
15–142-WA-S				0.39	16.56	61.38	3774.88	0.99	(c)
20–142-WA-S				0.30	18.15	61.17	3762.21	0.99	(c)
25–142-WA-S				0.25	24.89	61.48	3781.06	0.99	(c)*
30–142-WA-S				0.21	26.94	61.93	3808.89	1.00	(c)
5–142-WE-S	5.42	3	16.26	0.92	5.37	51.69	3179.18	0.81	(a), (a), (a)
10–142-WE-S				0.55	12.57	58.93	3624.35	0.92	(a), (c)*, (a)*
15–142-WE-S				0.39	16.84	59.55	3662.06	0.93	(c), (c), (c)*
20–142-WE-S				0.30	22.50	63.39	3898.38	0.99	(c), (c), (c)
25–142-WE-S				0.25	31.79	63.12	3881.80	0.99	(c), (c), (c)
30–142-WE-S				0.21	37.63	65.08	4002.34	1.02	(c), (c), (c)
5–85-WE-P	1.81	6	10.86	0.61	3.96	42.39	3903.55	0.94	(a), (a)*, (a)*, (a)*
10–85-WE-P				0.36	9.12	41.67	3836.96	0.92	(a)*, (a), (a), (a)
15–85-WE-P				0.26	18.55	41.37	3809.33	0.92	(a)*, (a), (a), (a)
20–85-WE-P				0.20	24.10	40.03	3685.91	0.89	(a), (a), (a), (b)*
25–85-WE-P				0.17	29.85	39.75	3660.11	0.88	(b)*, (b)*, (a), (a)
30–85-WE-P				0.14	30.79	39.83	3667.93	0.88	(b)*, (a), (a), (b)*
5–95-WA-P	3.62	3	10.86	0.61	5.21	36.74	3383.10	0.83	(b)
10–95-WA-P				0.37	8.30	40.27	3707.69	0.91	(a)
15–95-WA-P				0.26	12.79	37.16	3421.96	0.84	(a)
20–95-WA-P				0.20	18.63	37.24	3428.91	0.84	(b)
25–95-WA-P				0.17	15.65	39.15	3605.02	0.88	(b)
30–95-WA-P				0.14	10.28	36.32	3344.66	0.82	(a)
5–95-WE-P	3.62	3	10.86	0.61	2.89	30.62	2819.40	0.74	(b)*, (a), (a)
10–95-WE-P				0.37	6.33	35.69	3286.39	0.86	(b), (a), (a)
15–95-WE-P				0.26	8.25	35.00	3222.58	0.85	(b)*, (a), (b)*
20–95-WE-P				0.20	16.88	36.91	3398.39	0.89	(a), (b)*, (a)
25–95-WE-P				0.17	21.93	36.22	3334.84	0.87	(b), (b)*, (b)*
30–95-WE-P				0.14	21.39	34.04	3134.39	0.82	(b)*, (b)*, (b)*
5–142-WA-P	5.42	3	16.26	0.92	3.74	35.01	2152.86	0.61	(b)
10–142-WA-P				0.55	23.11	49.85	3065.87	0.86	(a)
15–142-WA-P				0.39	23.77	49.50	3044.00	0.86	(a)*
20–142-WA-P				0.30	23.04	43.44	2671.80	0.75	(a)
25–142-WA-P				0.25	28.03	50.92	3131.52	0.88	(a)
30–142-WA-P				0.21	27.50	52.41	3223.06	0.91	(a)
5–142-WE-P	5.42	3	16.26	0.92	3.56	40.76	2506.67	0.67	(b), (b), (b)
10–142-WE-P				0.55	10.58	48.49	2982.30	0.80	(a), (b), (a)
15–142-WE-P				0.39	23.67	48.12	2959.41	0.79	(a), (a), (a)*
20–142-WE-P				0.30	31.37	44.87	2759.35	0.74	(a)*, (b)*, (b)*
25–142-WE-P				0.25	39.00	52.51	3229.16	0.86	(b)*, (a)*, (a)*
30–142-WE-P				0.21	33.94	46.36	2850.94	0.76	(b)*, (b)*, (a)*

*excluded from data set.

specimen. The initial length of the section $l_{x,0}$ and the deformation measured along this section Δl_x were used to calculate the mean longitudinal strain ε_x during loading, which corresponds to the mean textile strain ε_t, while the load itself was divided by the fibre cross-sectional area of the longitudinal fibre strands $A_{tex,n}$ (see Table 4) to derive the corresponding textile stress σ_t. A representative stress–strain response is shown Fig. 5b in the right σ_t, ε_t quadrant. The peak-valley response indicates the development of a new transverse crack. The textile stress was also plotted as a function of the transverse strains ε_z, captured by the DIC measurements on the side of the specimens (Fig. 5b) in the left σ_t, ε_z quadrant. To calculate ε_z, transverse sections of regular intervals of 8 mm were generated (see Fig. 5a). The measured deformation $\Delta l_{z,i}$ of these sections was divided by the initial length $l_{z,i,0}$ of each section to calculate the strains $\varepsilon_{z,i}$. The onset of $\varepsilon_{z,i}$ corresponds to the development of splitting cracks. Together with the stress–strain relationships derived from the front surface, the stress state in the fibre strand at the initiation

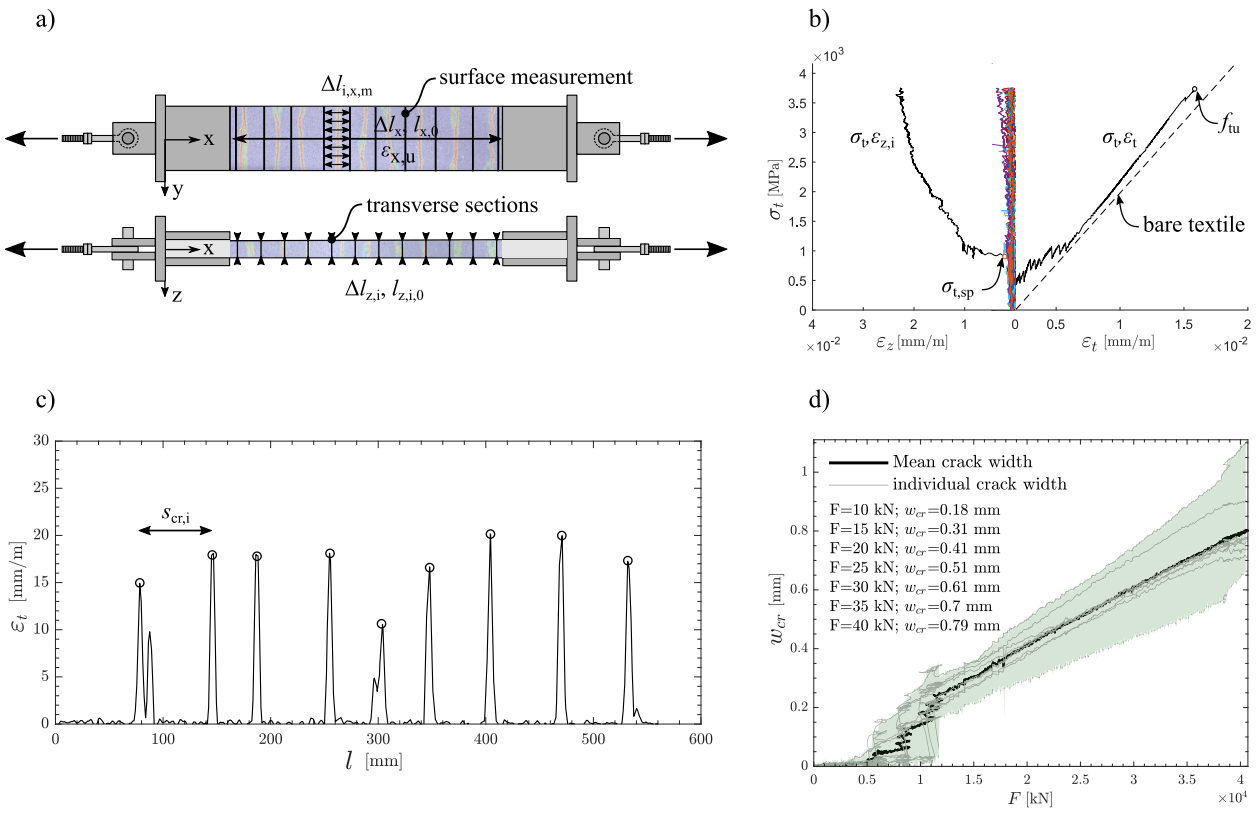

Fig. 5. Workflow for processing of data: Sections created on the DIC surfaces (section separation are not to scale) (a), stress–strain response of TRC-panels and transverse strain, where the onset of transverse strain indicates a splitting crack (b), crack distance before failure (end of stage III) (c) and crack width progression during loading (d).

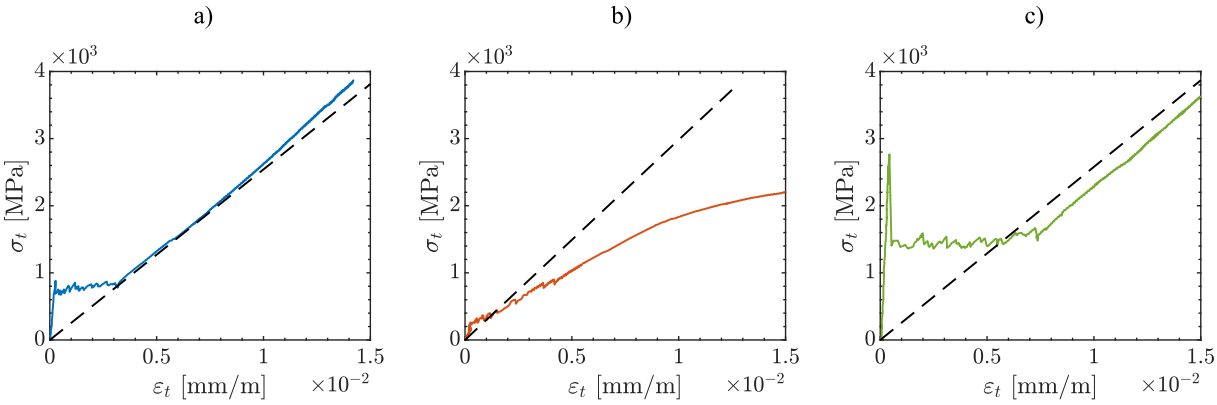

Fig. 6. Three representative sample responses observed during the uniaxial tensile tests: typical stress–strain relationship with uncracked stage, crack progression zone and stabilised cracking (a), slippage of the reinforcement due to anchorage failure (b) and load drop after initial crack due to progressive splitting cracking (c).

of the first longitudinal crack $\sigma_{t,sp}$ can therefore be evaluated, as shown in Fig. 5b.

Fig. 5c shows a plot of the strain profile along the testing length measured in the middle of the sample front surface right before the final failure of the sample. A significantly higher strain (peak) indicates a crack (the onset is defined when the strain becomes greater than the concrete failure strain, calculated from the data in Table 3). The position of the local peak maxima are then used to calculate the distances between the cracks $s_{cr,i}$, and the number of peaks gives the number of cracks n_{cr}. The average distance between cracks s_{cr} and the standard deviation are also calculated.

Finally, each transverse crack width $w_{cr,i}$ was derived from the DIC measurements by determining the mean value of length increase per crack $\Delta l_{i,x,m}$, and the average crack width w_{cr} is calculated and plotted together with the individual crack widths as a function of load (a typical example is shown Fig. 5d). To compare the crack widths w_{cr} of different specimens, the mean value and standard deviation thereof are extracted at seven different load stages.

2.4. Assessment of possible sources of errors

The quality of the data was checked to avoid any possible sources of error. A typical stress–strain response is depicted in Fig. 6a. While the specimen is uncracked, it shows a high stiffness and a linear elastic behaviour (stage I). When the tensile strength of the concrete is reached, primary cracks occur, gradually decreasing the system axial stiffness

Table 5
Main results of the uniaxial tensile tests (mean value μ ± standard deviation σ), $\sigma_{t,sp}$ is the tensile stress at first onset of an splitting crack, s_{cr} the mean value of the crack distance of the main cracks and $w_{cr,i}$ the crack width at load stage i (where i refers to load value).

	$\sigma_{t,sp}$ [MPa]	s_{cr} [mm]	$w_{cr,10}$ [mm]	$w_{cr,15}$ [mm]	$w_{cr,20}$ [mm]	$w_{cr,25}$ [mm]	$w_{cr,30}$ [mm]	$w_{cr,35}$ [mm]	$w_{cr,40}$ [mm]
5–85-WE-S	NaN	12.61 (±5.0)	0.07 (±0.03)	0.1 (±0.06)	0.12 (±0.06)	0.14 (±0.06)	0.16 (±0.06)	0.18 (±0.06)	0.21 (±0.07)
10–85-WE-S	1.1 (±0.05)	15.06 (±6.1)	NaN	0.13 (±0.07)	0.15 (±0.08)	0.18 (±0.09)	0.19 (±0.1)	0.21 (±0.11)	0.23 (±0.11)
15–85-WE-S	1.18 (±0.03)	22.57 (±7.8)	NaN	0.15 (±0.07)	0.19 (±0.08)	0.22 (±0.1)	0.27 (±0.11)	0.3 (±0.11)	0.35 (±0.13)
20–85-WE-S	1.29 (±0.08)	32.19 (±11.8)	NaN	0.3 (±0.06)	0.26 (±0.08)	0.32 (±0.1)	0.37 (±0.12)	0.43 (±0.12)	0.47 (±0.12)
25–85-WE-S	1.3 (±0.08)	32.71 (±12.6)	NaN	NaN	0.3 (±0.12)	0.33 (±0.13)	0.39 (±0.14)	0.42 (±0.16)	0.46 (±0.15)
30–85-WE-S	1.39 (±0.1)	45 (±16.8)	NaN	NaN	0.6 (±0.29)	0.68 (±0.3)	0.61 (±0.29)	0.65 (±0.24)	0.72 (±0.26)
5–95-WA-S[2]	NaN	NaN	NaN	NaN	NaN	NaN	NaN	NaN	NaN
10–95-WA-S	NaN	26.51 (±9.6)	NaN	0.11 (±0.04)	0.15 (±0.04)	0.19 (±0.05)	0.22 (±0.04)	0.25 (±0.05)	#WERT!
15–95-WA-S	1.32	20.2 (±9.1)	NaN	NaN	NaN	0.27 (±0.09)	0.31 (±0.11)	0.36 (±0.11)	0.4 (±0.13)
20–95-WA-S	1.51	29.44 (±10.8)	NaN	NaN	NaN	NaN	NaN	0.41 (±0.1)	NaN
25–95-WA-S	1.46	36.55 (±13.7)	NaN	NaN	NaN	0.34 (±0.16)	0.38 (±0.18)	0.44 (±0.19)	0.5 (±0.2)
30–95-WA-S	1.09	49.1 (±14.0)	NaN	NaN	0.41 (±0.1)	0.47 (±0.1)	0.56 (±0.13)	0.61 (±0.12)	0.73 (±0.2)
5–95-WE-S	NaN	22.55 (±9.3)	0.1 (±0.05)	0.13 (±0.07)	0.16 (±0.08)	0.2 (±0.1)	0.23 (±0.12)	0.26 (±0.13)	0.28 (±0.15)
10–95-WE-S	NaN	20.05 (±7.1)	NaN	0.14 (±0.06)	0.17 (±0.07)	0.21 (±0.08)	0.23 (±0.09)	0.26 (±0.09)	0.29 (±0.11)
15–95-WE-S	1.45 (±0.11)	19.78 (±10.0)	NaN	NaN	NaN	0.24 (±0.1)	0.27 (±0.11)	0.3 (±0.12)	0.34 (±0.13)
20–95-WE-S	1.41 (±0.07)	30.91 (±11.4)	NaN	NaN	NaN	NaN	0.39 (±0.13)	0.45 (±0.13)	0.52 (±0.15)
25–95-WE-S	1.46 (±0.08)	40.63 (±13.0)	NaN	NaN	NaN	NaN	0.49 (±0.18)	0.55 (±0.19)	0.59 (±0.16)
30–95-WE-S[2]	NaN	NaN	NaN	NaN	NaN	NaN	NaN	NaN	NaN
5–142-WA-S	NaN	19.73 (±8.4)	0.09 (±0.03)	0.12 (±0.04)	0.15 (±0.04)	0.18 (±0.06)	0.19 (±0.07)	0.21 (±0.08)	0.23 (±0.08)
10–142-WA-S	NaN	18.92 (±7.5)	NaN	0.11 (±0.04)	0.13 (±0.06)	0.14 (±0.06)	0.16 (±0.07)	0.17 (±0.08)	0.18 (±0.09)
15–142-WA-S	0.81	21.68 (±7.3)	NaN	NaN	0.13 (±0.06)	0.14 (±0.07)	0.16 (±0.08)	0.18 (±0.08)	0.21 (±0.1)
20–142-WA-S	0.85	43.58 (±13.2)	0.08 (±0.1)	0.09 (±0.17)	0.3 (±0.19)	0.34 (±0.2)	0.38 (±0.21)	0.44 (±0.23)	0.45 (±0.25)
25–142-WA-S[2]	NaN	NaN	NaN	NaN	NaN	NaN	NaN	NaN	NaN
30–142-WA-S	0.92	42.05 (±12.8)	NaN	NaN	NaN	NaN	0.37 (±0.21)	0.47 (±0.2)	0.52 (±0.23)
5–142-WE-S	NaN	21.1 (±7.8)	0.06 (±0.02)	0.08 (±0.03)	0.1 (±0.04)	0.11 (±0.04)	0.13 (±0.05)	0.15 (±0.06)	0.16 (±0.06)
10–142-WE-S[1]	1.35	19 (±6.9)	NaN	0.11 (±0.05)	0.14 (±0.06)	0.16 (±0.07)	0.19 (±0.08)	0.21 (±0.09)	0.24 (±0.09)
15–142-WE-S	1 (±0.11)	21.14 (±9.9)	0.05 (±0.05)	0.11 (±0.12)	0.14 (±0.07)	0.16 (±0.08)	0.18 (±0.09)	0.2 (±0.09)	0.22 (±0.1)
20–142-WE-S	0.97 (±0.04)	33.56 (±12.0)	NaN	NaN	0.32 (±0.11)	0.31 (±0.11)	0.36 (±0.16)	0.41 (±0.19)	0.45 (±0.21)
25–142-WE-S	1.06 (±0.03)	39.58 (±16.1)	NaN	NaN	NaN	NaN	0.42 (±0.16)	0.44 (±0.17)	0.49 (±0.18)
30–142-WE-S	0.99 (±0.08)	48.56 (±18.1)	NaN	NaN	NaN	NaN	NaN	NaN	0.67 (±0.33)
5–85-WE-P	1 (±0.2)	48.34 (±21.4)	0.17 (±0.09)	0.29 (±0.08)	0.37 (±0.11)	0.45 (±0.14)	0.53 (±0.17)	0.61 (±0.2)	0.69 (±0.23)
10–85-WE-P	1.98 (±0.5)	67.55 (±22.1)	0.13 (±0.14)	0.26 (±0.23)	0.45 (±0.26)	0.58 (±0.33)	0.68 (±0.3)	0.76 (±0.34)	0.84 (±0.45)
15–85-WE-P	1.59 (±0.22)	70.44 (±27.5)	NaN	NaN	0.17 (±0.26)	0.54 (±0.38)	0.79 (±0.32)	0.91 (±0.33)	1.06 (±0.36)
20–85-WE-P	1.27 (±0.22)	85.78 (±29.6)	NaN	NaN	0.59 (±0.57)	1.17 (±0.6)	1.13 (±0.61)	1.45 (±0.71)	1.68 (±0.85)
25–85-WE-P	1.02 (±0.14)	98.23 (±22.0)	NaN	NaN	NaN	1.14 (±0.51)	1.3 (±0.77)	1.55 (±0.77)	1.73 (±0.79)
30–85-WE-P[1]	0.87	107.74 (±35.4)	NaN	NaN	NaN	1.26 (±0.3)	1.47 (±0.35)	1.67 (±0.39)	1.94 (±0.66)
5–95-WA-P	NaN	45.98 (±22.8)	0.29 (±0.06)	0.33 (±0.12)	0.45 (±0.16)	0.49 (±0.24)	0.57 (±0.27)	0.66 (±0.31)	NaN
10–95-WA-P	NaN	118.91 (±31.1)	NaN	0.58 (±0.01)	0.82 (±0.05)	1.03 (±0.06)	1.09 (±0.4)	1.27 (±0.42)	1.42 (±0.44)
15–95-WA-P	1.98	133.26 (±22.6)	NaN	NaN	NaN	1.22 (±0.89)	1.51 (±1.11)	2.11 (±1.37)	NaN
20–95-WA-P	1.62	183 (±44)	NaN	NaN	NaN	1.39 (±0.27)	1.76 (±0.49)	1.93 (±0.53)	NaN
25–95-WA-P	0.88	183.55 (±5.9)	NaN	NaN	1.03 (±0.49)	1.3 (±0.51)	1.6 (±0.58)	2.02 (±0.72)	NaN
30–95-WA-P	1.01	255.56 (±21.2)	NaN	0.74 (±0.25)	1.72 (±0.38)	2.34 (±0.08)	2.83 (±0.06)	3.07 (±0.14)	NaN
5–95-WE-P	NaN	70.95 (±23.7)	0.28 (±0.07)	0.39 (±0.12)	0.52 (±0.17)	0.64 (±0.21)	0.76 (±0.27)	NaN	NaN
10–95-WE-P	NaN	109.65 (±41.9)	0.18 (±0.16)	0.56 (±0.1)	0.83 (±0.21)	0.96 (±0.28)	1.12 (±0.3)	1.43 (±0.37)	NaN
15–95-WE-P	1.1 (±0.11)	188.7 (±58.8)	NaN	NaN	1.08 (±0.21)	1.16 (±0.4)	1.45 (±0.42)	3.12 (±1.68)	NaN
20–95-WE-P	1.85 (±0.39)	237.14 (±78.39)	NaN	NaN	1.15 (±0.28)	1.39 (±0.16)	1.94 (±0.69)	3.35 (±0)	NaN
25–95-WE-P	2.06 (±0.64)	206.27 (±73.01)	NaN	0.86 (±0.03)	1.17 (±0.09)	1.4 (±0.19)	2.67 (±1.36)	3.12 (±1.64)	NaN
30–95-WE-P[2]	NaN	NaN	NaN	NaN	NaN	NaN	NaN	NaN	NaN
5–142-WA-P	NaN	35.93 (±10.5)	0.17 (±0.05)	0.17 (±0.06)	0.2 (±0.06)	0.24 (±0.06)	0.29 (±0.07)	NaN	NaN
10–142-WA-P	NaN	54.26 (±20.5)	NaN	NaN	NaN	0.45 (±0.28)	0.53 (±0.31)	0.58 (±0.31)	0.65 (±0.31)
15–142-WA-P[2]	NaN	NaN	NaN	NaN	NaN	NaN	NaN	NaN	NaN
20–142-WA-P	0.81	71.12 (±31.1)	NaN	NaN	NaN	0.38 (±0.25)	0.56 (±0.39)	0.76 (±0.52)	0.88 (±0.59)
25–142-WA-P	0.81	75.29 (±16.4)	NaN	NaN	NaN	NaN	0.6 (±0.05)	0.72 (±0.08)	0.83 (±0.12)
30–142-WA-P	0.73	78.12 (±4.5)	NaN	NaN	NaN	0.54 (±0.15)	0.66 (±0.19)	0.73 (±0.18)	0.81 (±0.17)
5–142-WE-P	NaN	53.78 (±26.8)	0.15 (±0.07)	0.21 (±0.08)	0.26 (±0.1)	0.32 (±0.12)	0.36 (±0.14)	0.41 (±0.16)	0.37 (±0.17)
10–142-WE-P	1.29 (±0.63)	115.79 (±31.5)	NaN	0.48 (±0.22)	0.48 (±0.18)	0.64 (±0.15)	0.78 (±0.19)	0.99 (±0.31)	1.13 (±0.39)
15–142-WE-P	1.49 (±0.32)	154.62 (±47.0)	NaN	NaN	NaN	0.68 (±0.48)	0.83 (±0.52)	1.17 (±0.24)	1.48 (±0.39)
20–142-WE-P[2]	NaN	NaN	NaN	NaN	NaN	NaN	NaN	NaN	NaN
25–142-WE-P[2]	NaN	NaN	NaN	NaN	NaN	NaN	NaN	NaN	NaN
30–142-WE-P[2]	NaN	NaN	NaN	NaN	NaN	NaN	NaN	NaN	NaN

[1] only one specimen with valid data.
[2] no specimen with valid data.

with each new crack (stage II or crack progression zone). This stage ends when no further crack initiates. The third stage (stabilised cracking or stage III), is characterised by a linear elastic behaviour until ultimate failure due to rupture of the textile [28,35]. The stiffness in this stage is the stiffness of the bare textile, with an offset due to tension-stiffening [36]. Slight deviations may occur due to the scatter in the material properties. This type of failure is referred to as failure mode (a).

In some cases, however, the reinforcement showed a deviation from the nominal position in the centre of the specimen, therefore inducing a bending moment that affected the cracking behaviour. This manifested in an uneven strain distribution in the transverse direction. If the difference of the top and bottom strains at the beginning of the stabilized cracking zone was higher than ± 0.10 mm/m, specimens were excluded from the data set. These specimens accounted for about 8.3% of all

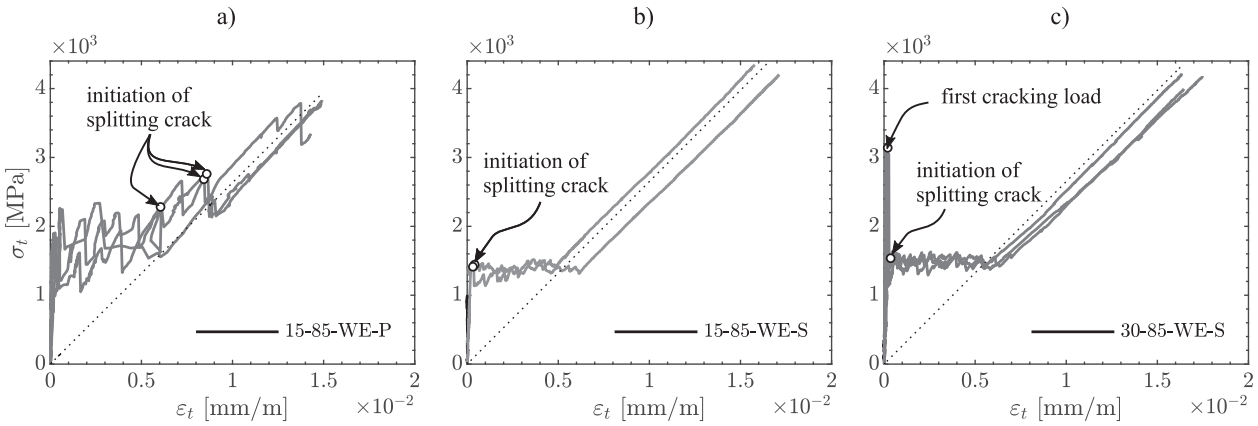

Fig. 7. Stress-Strain response of specimens 15–85-WE-P (a), 15–85-WE-S (b) and 30–85-WE-S (c).

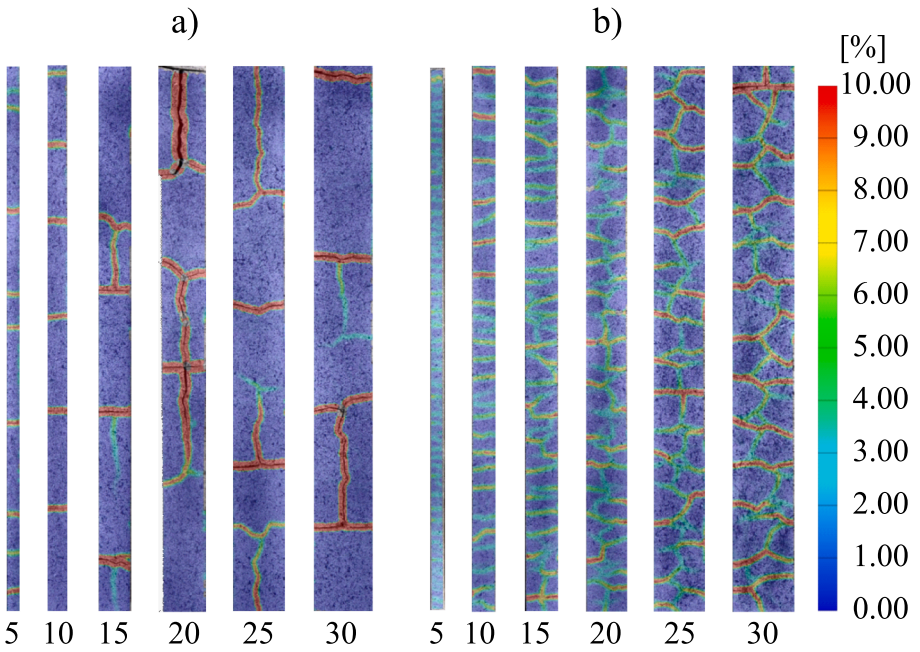

Fig. 8. Splitting cracking behaviour for a concrete cover thickness ranging from 5 to 30 mm for textile type 95 plain (a) and sand-coated (b). Images taken during stage III.

specimens. Another possible source of error is the clamping of the specimens. Indeed, an anchorage failure of the reinforcement (failure mode b) was observed in some specimens, where the reinforcement was pulled out of the anchorage zone (see Fig. 6b). If such a failure occurred during stages I and II, the data was excluded from the data set (this accounted for another 11.8% of the tests). If, however, the anchorage failure occurred when the specimen was already in stage III (indicating a good utilisation of the reinforcement), the crack distance and also the crack width were processed up to the point where anchorage failure occurred. The crack width at higher load stages was nonetheless excluded from the test data.

An interesting effect can be seen in Fig. 6c, where a significant drop in reinforcement stress was observed at the onset of the first crack. While this was initially attributed to errors in the test data, the DIC measurements from the side of the specimen revealed that this effect was due to the propagation of a longitudinal crack in the specimen and thus represents a realistic scenario. This phenomenon was referred to as failure mode (c) and is discussed further in the results section. After the exclusion of different samples for the reasons mentioned previously, a total of 95 specimens remained in the dataset. In almost all cases, at least one of the repeat specimens provided valid data (except for the Warp fibre strands, where only one specimen was tested). This allows for a reliable evaluation of the cracking behaviour of TRC.

3. Results

Table 5 lists the core results for the individual series (mean values and standard deviation). As defined previously, $\sigma_{t,sp}$ is the reinforcement stress at the onset of the first splitting crack, as determined from the side strain measurements perpendicular to the reinforcement layer, s_{cr} is the average crack distance between the individual transverse (main) cracks on the front surface of the specimens right before the failure of the sample (end of stage III). The continuous measurement of the average crack width w_{cr} was evaluated selectively at load stages 10 kN: 5 kN: 40 kN (initial load stage: load step: max load stage), and is referred to as $w_{cr,10}$ - $w_{cr,40}$ in Table 5. NaN indicates that no measurement of crack width was achievable: either no crack had occurred at that load stage – note that the load at first cracking increases with increasing concrete cover (decreasing reinforcement ratio) – or the specimen failed prior to that load stage.

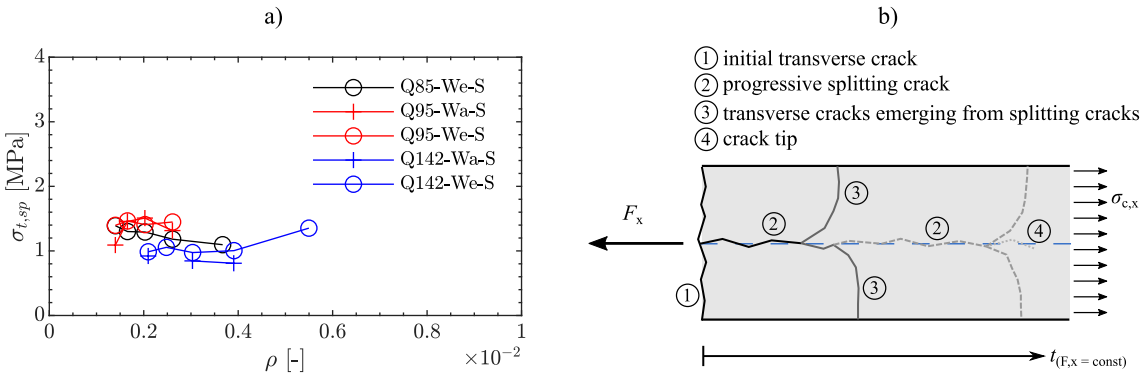

Fig. 9. Splitting tensile behaviour of sand-coated textiles: Textile reinforcement stress at the initiation of a splitting crack $\sigma_{t,sp}$ (a) and side view of splitting crack progression and emergence of new transverse crack from the crack tip of the splitting crack (b).

In the case of the warp direction, no results were obtained for series 25–142-WA-S; 5–95-WA-S; 15–142-WA-P, as the single specimen did not lead to reliable results. In the weft direction, series 30–95-WE-S, 30–95-WE-P and 20–142-WE-P, 25–142-WE-P, 30–142-WE-P could not be evaluated due to an excessive spalling of the concrete cover right after the first cracks occurred. However, since the overall data is comprehensive, the information loss is marginal.

To gain greater insight into the cracking behaviour and to assess the differences between the individual series, the results are analysed in more detail in the following sections. This analysis includes (a) the stress–strain response of the specimens, (b) the splitting cracking behaviour of the individual series and the reinforcement stress at the initiation of splitting cracking, (c) a comparison of the normalised crack distance and (d) the crack width progression during loading. Some of the results of series 142 have already been presented elsewhere [37] but will be discussed in more detail here.

3.1. Stress-Strain response

The stress–strain response for all specimens is given in Annex A. For the sake of clarity, only representative specimens with distinct features are presented in this section. As already described in Section 2.4, the response under tensile loading typically undergoes three stages – uncracked (stage I), crack progression (stage II) and stabilized cracking (stage III) – with the offset between the stress–strain response of the bare textile and the specimen being the tension stiffening effect.

In the plain textile samples, such an offset between the stress–strain response of the reinforced specimens and the bare textile (dotted line in Fig. 7) was observed, but gradually decreased when splitting cracks appeared; see for example Fig. 7a. In contrast, limited or no tension stiffening was observed in the sand-coated textiles (Fig. 7b). This suggests a debonding between the textile and the concrete as a result of splitting cracking at low stress levels σ_t (see also section 3.2). A slight offset in stress, below the stress–strain response of the bare textile, as can be seen in Fig. 7b for one specimen, additionally indicates sliding between the textile and the surrounding concrete during the longitudinal cracking process. Furthermore, when comparing specimens with different concrete covers, it was found that the stress–strain response of the specimens with sand-coated fabrics was almost independent of the cover thickness. This is perplexing since the concrete cross-section resistance F_{cr} increases with cover thickness. However, after the first main crack occurred, the stress dropped to a similar stress level σ_t for all samples. This behaviour can be seen for example in Fig. 7c, where there is a distinct peak at the end of stage I. The above-mentioned behaviour was not observed for textiles with a plain surface, indicating that the bond behaviour differs between the sand-coated and the plain textiles.

3.2. Splitting cracking behaviour

The DIC-observations on the side of the specimens enabled the evaluation of the loading stage at crack initiation along the layer of the textile reinforcement (see Table 5 – $\sigma_{t,sp}$). Splitting cracks did not generally occur in specimens with a concrete cover below 15 mm although there were a few exceptions. At or above a cover thickness of 15 mm, longitudinal cracking occurred regardless of the textile surface finish. In Fig. 8, the splitting cracking behaviour for textile type 95 is shown for different cover values and fibre strand surface finish.

It is apparent that the cracking process differs depending on the textile surface. For the sand-coated textiles, it was observed that if longitudinal cracking happened it initiated immediately after the first main crack occurred. In Fig. 9a, the corresponding stress state at the onset of longitudinal cracking in the respective sand-coated specimens was plotted as a function of the reinforcement ratio. It can be seen that it is roughly the same for all the textile types and corresponds to the stress level in the crack progression zone, which was independent of the cover thickness (Fig. 7b and c). Subsequently, the longitudinal crack propagates at an essentially constant stress level along the reinforcement layer, with new transverse cracks initiating from the tip of the longitudinal crack (see Fig. 9b).

In the case of specimens with plain textiles, longitudinal cracking primarily occurred in the stabilised cracking zone of the stress–strain diagram, with the load stage at the initiation of a splitting crack increasing somewhat with increasing reinforcement ratio. However, no clear trend was observable in this case and this behaviour might also be attributable to the scatter in the geometric properties of the plain textiles. It is worth noting that the longitudinal cracking was accompanied by an excessive spalling of the concrete cover only in the case of plain textiles.

3.3. Crack distance

When a transverse crack occurs, the load within the crack is solely carried by the reinforcement. Starting from the crack edges, the tensile load is progressively transferred back to the concrete through bond stresses. The distance between the crack edge and the location where the strains in the concrete and in the reinforcement are equal, is called the transfer length. Considering a stochastic distribution of local concrete tensile strengths within the sample, transverse cracks in case of the plain textiles occurred randomly along the specimen, and the distance between cracks is smaller than twice the transfer length. The crack distance is therefore correlated with the transfer length and gives information on the bond performance of the reinforcement: a better bond performance leads to smaller crack distances, while a weaker bond results in larger crack distances. For sand-coated textiles with a concrete cover equal or larger than 15 mm, a different behaviour was observed due to the

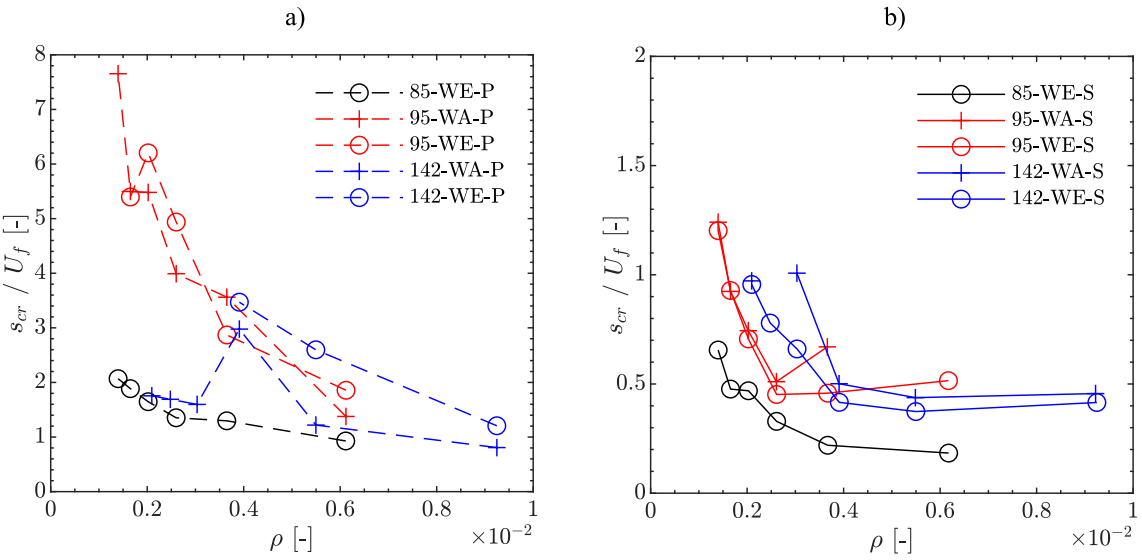

Fig. 10. Comparison of the crack distance s_{cr} normalised by the fibre strand circumference U_f versus the reinforcement ratio ρ: plain textiles displayed in dashed lines (a) sand-coated textiles displayed in continuous lines (b).

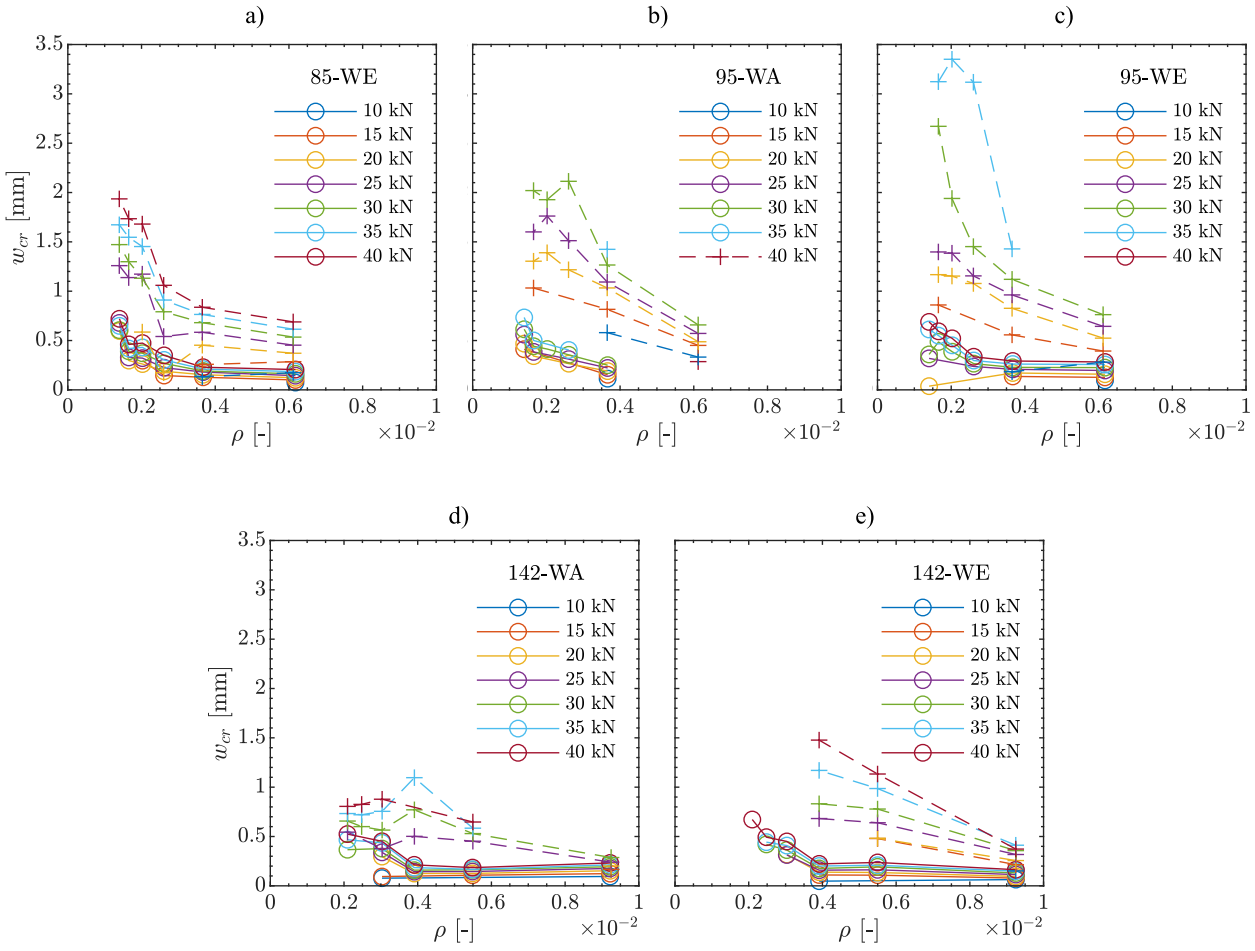

Fig. 11. Crack width progression in dependency of the reinforcement ratio for the plain (dotted lines) and sand-coated (continuous lines) textiles: 85-WE (a), 95-WA (b), 95-WE (c), 142-WA (d) and 142-WE (e).

longitudinal crack propagation that initiated from the first transverse crack. This suggests that in this case there is no direct correlation between the transfer length and the crack distance. However, the cracking process itself is dependent upon the bond performance, thus the comparison of the crack distance for different textiles also allows for inferences about the bond performance.

To compare fibre strands with different circumferential properties and hence contact areas with concrete, the crack distances for each

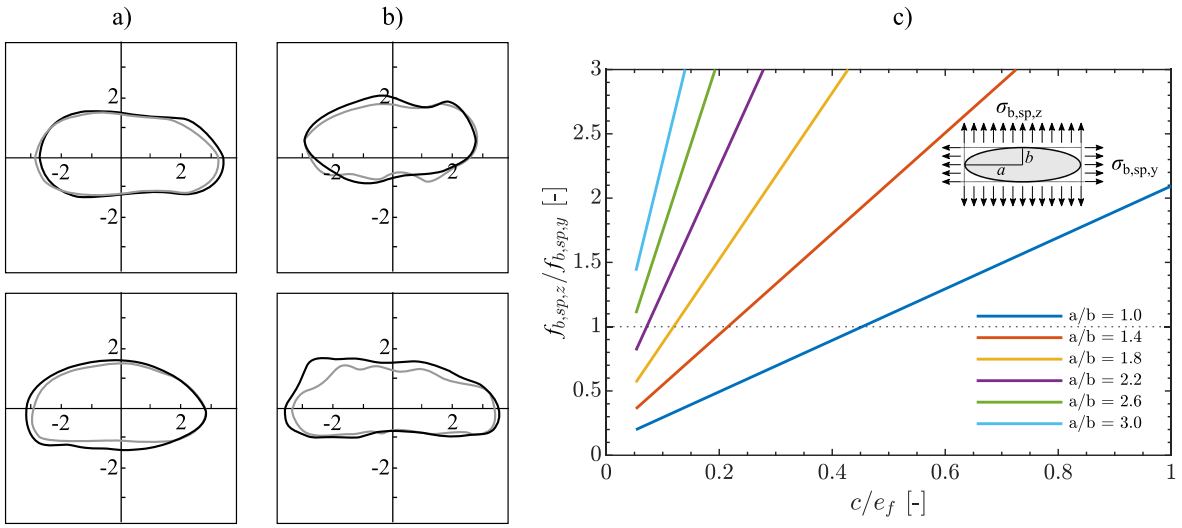

Fig. 12. Cross-sectional shape of fibre strand type Q142 in warp direction (top) and weft direction (bottom) for the uncoated (a) and sand-coated (b) textiles [39]. The cross-section displayed in black colour is the cross-section at the intersection with the transverse strands, while the light-grey one displays the cross-section in the middle between two intersections. The ratio of splitting tensile stresses due to bond action $\tau_{b,sp,z}$ / $\tau_{b,sp,y}$ in dependency of the fibre strand cross-section geometry (ratio a/b of ellipse axis) and the ratio of concrete cover thickness c to centre-to-centre distance of the fibre strands e_f (c) [40].

series were normalised with respect to the fibre strand circumference U_f (see Table 1). The normalised average crack distance s_{cr} / U_f as a function of the reinforcement ratio is depicted in Fig. 10 for the plain (Fig. 10a) and sand-coated (Fig. 10b) textiles.

The results show that all the sand-coated fibre strands have a significantly higher bond performance than the plain strands (noting the different axis scales), although splitting cracks occurred very early in the case of concrete covers equal to or bigger than 15 mm. The results also show that the normalised crack distance for the plain textiles increases almost exponentially with decreasing reinforcement ratio (increasing concrete cover) (R^2-value of 0.93 for an exponential fit). This can be attributed to two effects: with increasing concrete cover thickness, the concrete cross-section exhibits higher tensile resistance, which leads to a longer transfer length (see Fig. 1d). Secondly, the mean value of the bond stresses usually decreases with an increased transfer length. The exponential fit, however, is not very accurate for the sand-coated textiles, with an R^2 value of only 0.60. In fact, the occurrence of splitting cracks in specimens with lower reinforcement ratios ρ decouples the crack distance from the transfer length and leads to an almost linear growth for decreasing reinforcement ratio. This was only apparent in the sand-coated fabric plot, since the splitting cracks in this case usually initiated immediately after the first main cracks occurred, leading to a commensurate decrease in bond performance.

While all the sand-coated textiles generally show a high bond stiffness, two series with plain reinforcement, namely 85-WE-P and 142-WA-P exhibit a significantly better bond performance (as indicated by a lower s_{cr} / U_f ratio) than the other plain textiles. In the particular case of series 142, there was even a significantly different bond behaviour between the weft and warp direction. This tends to show that the fabrication process of the textiles has a substantial influence on the bond performance of plain textiles. This observation will be addressed in more detail in section 4.1.

3.4. Crack width

To study the influence of the concrete cover on the cracking behaviour, the crack width progression of the individual series was plotted as a function of the reinforcement ratio (Fig. 11). The crack width corresponds to the integral of the strain difference between the concrete and the textile reinforcement along the transfer length plus the strain of the fibre strand due to load. This implies that the TRC-samples with plain textiles, which exhibited larger crack distances when loaded (for a given reinforcement ratio) also have wider cracks, whereas the sand-coated fibre strands should exhibit small crack widths, which is favourable for the serviceability limit state. This is clearly visible in Fig. 11, where the crack width of the specimens with plain textiles is up to three times higher than that of the samples with the sand-coated textiles. Considering an allowable crack width in the range of 0.4–0.7 mm, as suggested in ACI 440.1R-15 [38] for FRP reinforcement, the crack width of the plain textiles may become a controlling criterion when designing TRC-elements. Within the plain textiles, however, the type 85 reinforcement shows the smallest crack width, being up to 2.5 times smaller compared to the other plain textiles, highlighting features that positively influence the bond performance. The plots also reveal a distinct transition in the crack widths at concrete covers of 15 mm (reinforcement ratio $\rho = 0.26$ in sample types 85 and 95 and $\rho = 0.39$ for sample type 142). Significantly increased crack widths were observed at and below these reinforcement ratios. As described in the previous section, this transition corresponds to the occurrence of splitting cracks. These results confirm that the appearance of longitudinal cracks is responsible for a decrease in bond performance. A seemingly contradictory behaviour was observed for plain textile type 95 and 142 WA, where the crack widths below this critical reinforcement ratio seem to remain at a constant level. The DIC observations shed some light on this phenomenon, showing secondary transverse cracks propagating from the tip of the splitting cracks at higher load stages. These additional cracks lead to smaller crack distances and crack widths, which in this case are not representative of an increased bond strength but in fact are the consequence of a significantly decreased bond strength.

4. Discussion on the cracking behaviour

The following section discusses aspects that emerged from the systematic investigation described in this paper.

4.1. Differences between fibre strands

A significant difference between the bond behaviour of sand-coated and plain fibre strands was typically observed. It is evident that the additional sand-coating increases the roughness of the fibre strand surface and enables greater interlock with the concrete, thus leading to small crack distances and crack widths. In general, larger crack widths

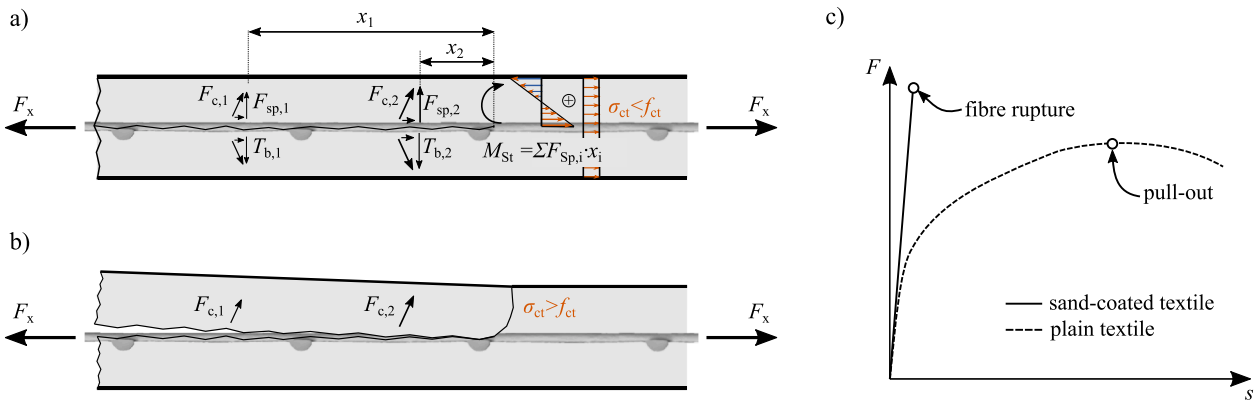

Fig. 13. Splitting vs spalling: stress distribution at the crack tip due to wedge effect $F_{c,i}$ and splitting action $F_{sp,i}$ along the reinforcement (a) and secondary crack formation that occurs if the tensile stresses σ_{ct} at the crack tip surpass the concrete tensile strength f_{ct} (b). M_{sp} is the bending moment caused by the wedge effect and x_i is the lever arm between splitting force $F_{sp,I}$ and crack tip. Pull-out force and slip relationship of sand-coated and plain fibre strands obtained from pull-out tests (c) [39].

were observed for the plain textiles, except for two plain fibre strands, namely 85-WE and 142-WA. The laser scans shown in Fig. 3 revealed that neither the fibre strand type 85 nor 142 exhibits a pronounced regularly repeating variation in terms of the cross-sectional dimensions. Thus, this geometric feature cannot explain the improved cracking behaviour. It is therefore postulated that the better bond performance of the specimens of type 142-WA-P is due to the rough surface created by the knitting technique used for this type of reinforcement (tricot binding with a needle offset). This ribbed surface is not present in the case of the warp fibre strand of type 95, which is knitted using double-tricot binding. In the case of textile type Q85-WE-P, the improved behaviour is partially attributed to the much stiffer connection between strands, linked to the higher resin content of this newer generation of textiles. This contrasts with previous investigations where the knot resistance between weft and warp fibre strands was negligible [25]. Additionally, the cross-sectional area and centre-to-centre distance between the fibre strands is smaller compared to the other textile types, leading to a larger number of transverse fibre strands. This emphasizes the importance of the design and processing of textile reinforcement, where small details can have a significant impact on the bond stiffness and strength.

4.2. Longitudinal crack progression

During the experimental campaign, the initiation of a longitudinal crack in the layer of the textiles was observed at larger concrete covers (low reinforcement ratios) for all the textiles studied here. Preinstorfer and Kromoser [22] identified that the fibre strand elliptical cross-sectional geometry and the regularly repeating variation in cross-sectional dimensions are the main parameters that cause such splitting cracks. While the repeating variation is only lightly pronounced in the present fibre strands, they still have a distinct elliptical shape even when sand-coated. An example for Q142 is shown in Fig. 12a and b.

The possibility that the splitting crack may instead appear perpendicular to the reinforcement layer in samples with a small concrete cover was not confirmed experimentally. Further studies by the authors on this topic were carried out using lower and upper bound considerations [40], see Fig. 12c. In this plot, the ratio of $\sigma_{b,sp,z}$ / $\sigma_{b,sp,y}$ describes the unequal splitting stress distribution along the perimeter of the fibre strand due to the elliptical cross-sectional shape. Since the direction of a longitudinal cracking is dependent upon the concrete resistance either in the width or thickness direction (whatever is smaller) the ratio of $f_{b,sp,z}$ / $f_{b,sp,y}$ is plotted as a function of the width (centre-to-centre distance) and the thickness (concrete cover). The results show that for the textiles used in this study, which have an elliptical shaped cross-section with an a/b ratio between 2 and 3 and a centre-to-centre distance of the fibre strand $e_f \geq 21$ mm, a longitudinal crack perpendicular to the reinforcement layer is not predicted to occur for concrete covers thicker than 3 mm, therefore confirming the observations from the experimental campaign.

4.3. Splitting vs spalling

The splitting cracking behaviour was observed to significantly depend upon the textile surface finish. For the sand-coated textiles with a concrete cover bigger than 10 mm, a splitting crack initiated at low load levels, independently of the cover thickness (see Fig. 9). The splitting crack propagated throughout the whole specimen, and eventually new transverse cracks emerged from the splitting crack tips. However, the concrete cover remained intact at higher loads and did not detach. In the case of the plain textiles, no such progressive splitting cracking was observed and the transverse cracks occurred randomly along the specimen. However, splitting cracks emerged at later load stages leading to an excessive spalling of the concrete cover. The spalling led to a complete detachment of the concrete even at loads that were much lower than the failure capacity of the fibre strands. Although the behaviour is different from the sand-coated textiles, a similar mechanism is suspected to be the cause: The splitting tensile force (depicted in Fig. 13 as the resulting splitting force per mesh width $F_{sp,I}$ calculated by integrating the splitting tensile stresses with respect to the mesh surface area) that is oriented perpendicular to the layer of the textile reinforcement results in a bending moment at the crack tip $M_{sp} = \Sigma F_{sp,i} \cdot x_i$. If the concrete tensile stress σ_{ct} at the crack tip stemming from this bending moment, superimposed with the tensile stresses due to uniaxial tension, eventually surpasses the tensile strength of the concrete, new transverse cracks occur (see Fig. 13a). Because of the superior bond performance of the sand-coated textiles (see Fig. 13c) and the unfavourable splitting stress distribution, as a result of their elliptical shape, splitting cracks occur even before the full tensile force is transferred back to the concrete and new transverse cracks emerge from the crack tip of these splitting cracks. This leads to the distinct stress drops in the stress–strain responses which were observed for concrete covers $c \geq 15$ mm (see Section 3.1 and Annex A). Due to the superior interlock between the fine quartz sand particles and the concrete, the concrete cover does not detach, however, minimal or no tension stiffening can be exploited. In the case of the plain fabrics and their lower bond stiffness (see Fig. 13c), the tensile stress in the textile is fully transferred back to the concrete after the initiation of the transverse crack, leading to further primary cracks at distances between one and two times the transfer length, similar to steel-reinforced concrete. However, once a splitting crack appears in the stabilized cracking stage, the slightest repeating variation in the cross-sectional dimensions acts as a wedge and splits apart the concrete cover. In the case of large crack spacings, this can be accompanied by secondary crack development (see Fig. 13b). Additional wedge effects

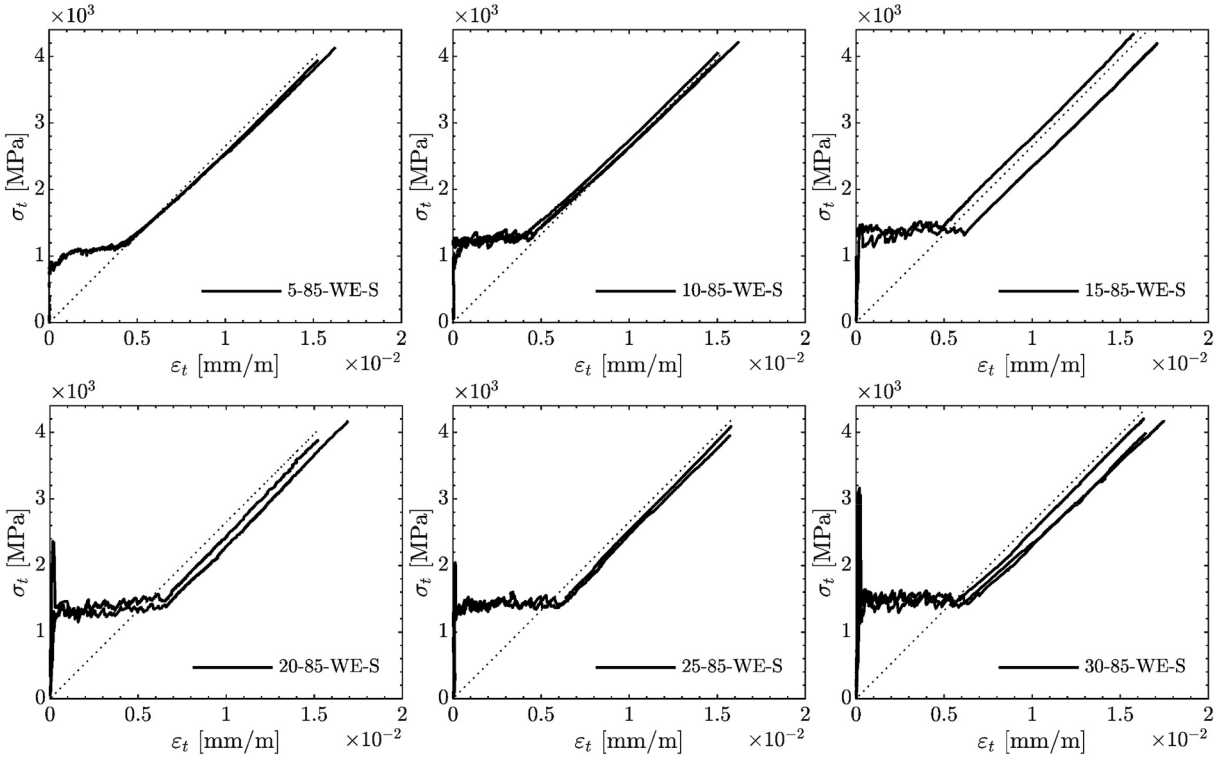

Fig. A1. Stress-Strain Response of Specimens type 85-WE-S.

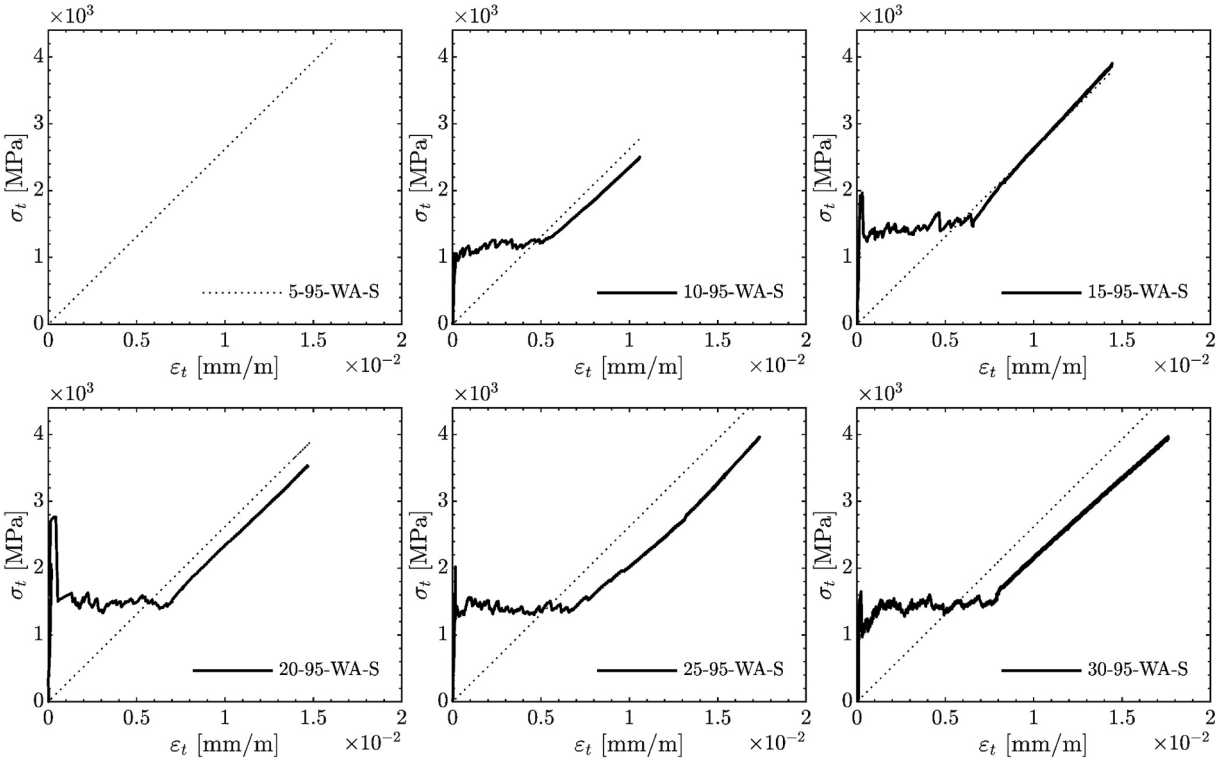

Fig. A2. Stress-Strain Response of Specimens type 95-WA-S.

can also arise from the transverse fibre strands pushing against the concrete cover.

When splitting cracks do not lead to subsequent failure, e.g. anchorage [15] or shear failure [16], it is concluded that splitting cracks could be acceptable if the reduction in the bond performance and in tension stiffening are reliably predictable, the crack widths remain small and the overall bearing capacity is not affected by those cracks. If textiles, however, tend to induce a spalling of the concrete cover, additional measures must be taken to avoid spalling at least in the serviceability limit state.

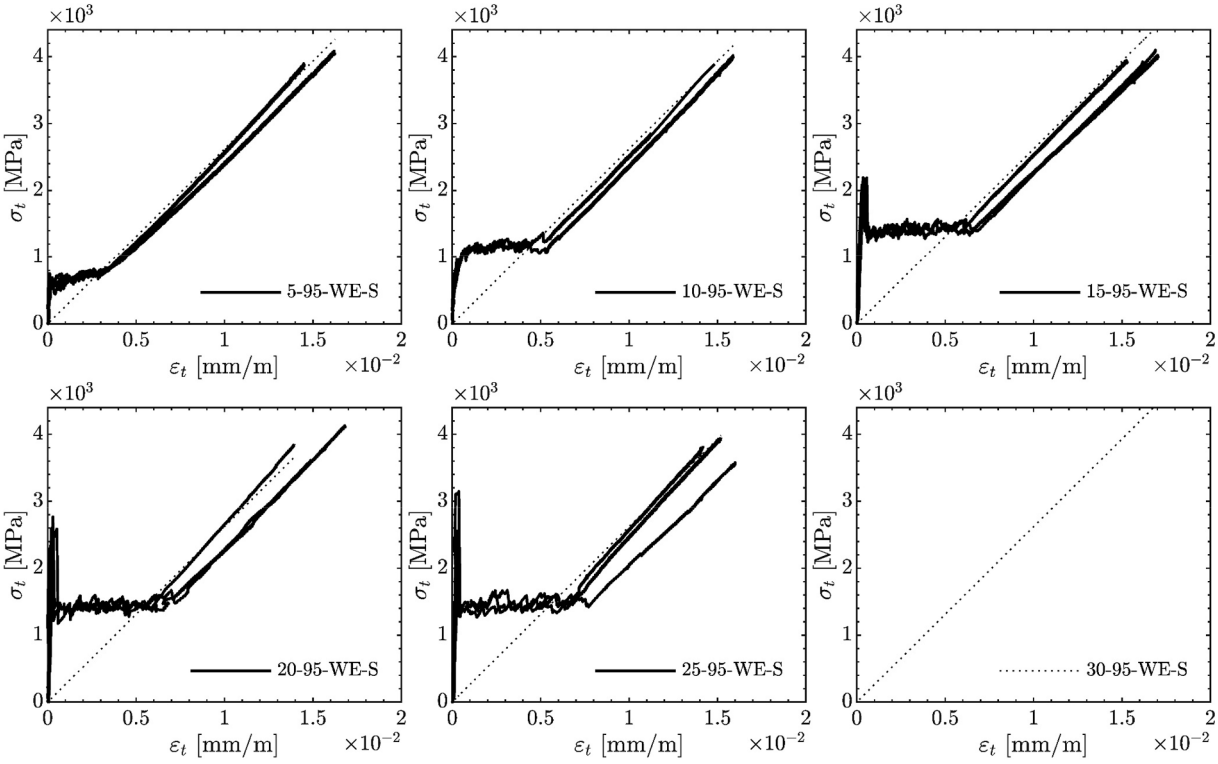

Fig. A3. Stress-Strain Response of Specimens type 95-WE-S.

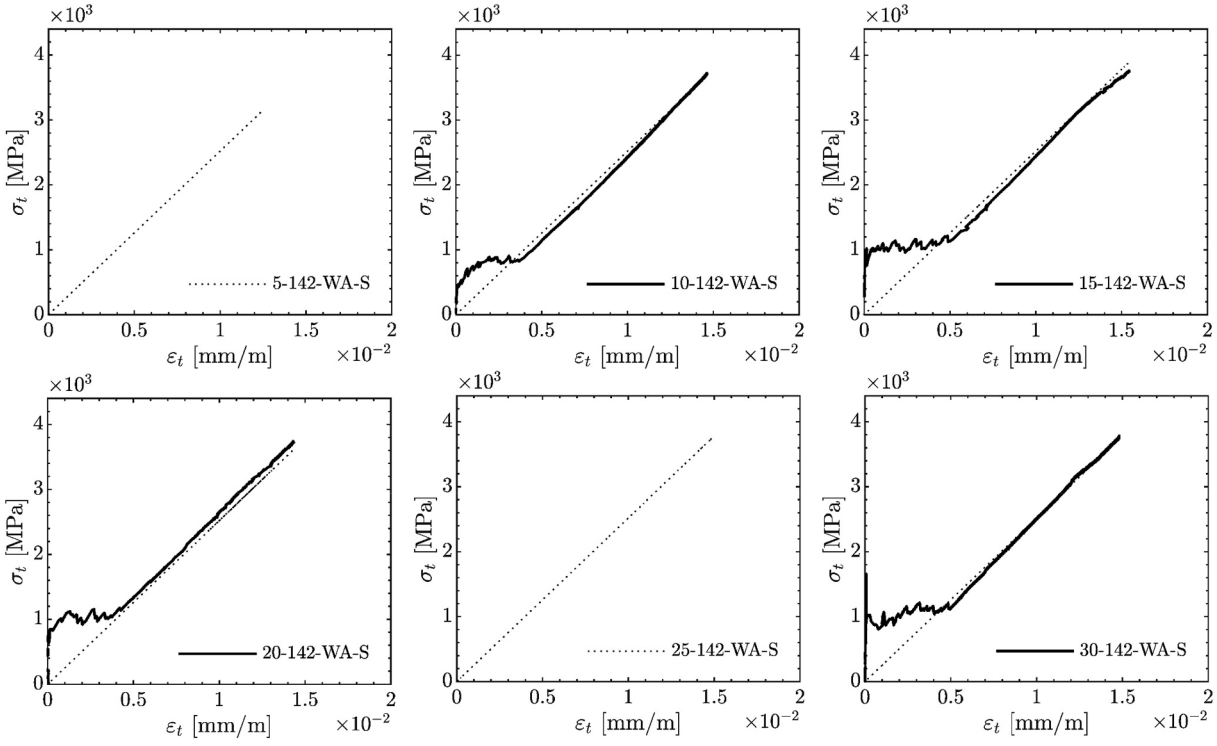

Fig. A4. Stress-Strain Response of Specimens type 142-WA-S.

4.4. ρ_{min} to avoid splitting in thin-walled elements

As the occurrence of a splitting crack appears to be directly related to the reinforcement ratio (or concrete cover thickness), a critical reinforcement ratio can be introduced. If the actual reinforcement ratio is below this critical value, the bond performance must be reduced, or additional measures must be taken to prevent spalling of the concrete cover. The ratio should be taken as the reinforcement ratio ρ of the concrete tensile area affected by the reinforcement. In the case of beams subjected to flexure, for example, this ratio differs from the ratio that

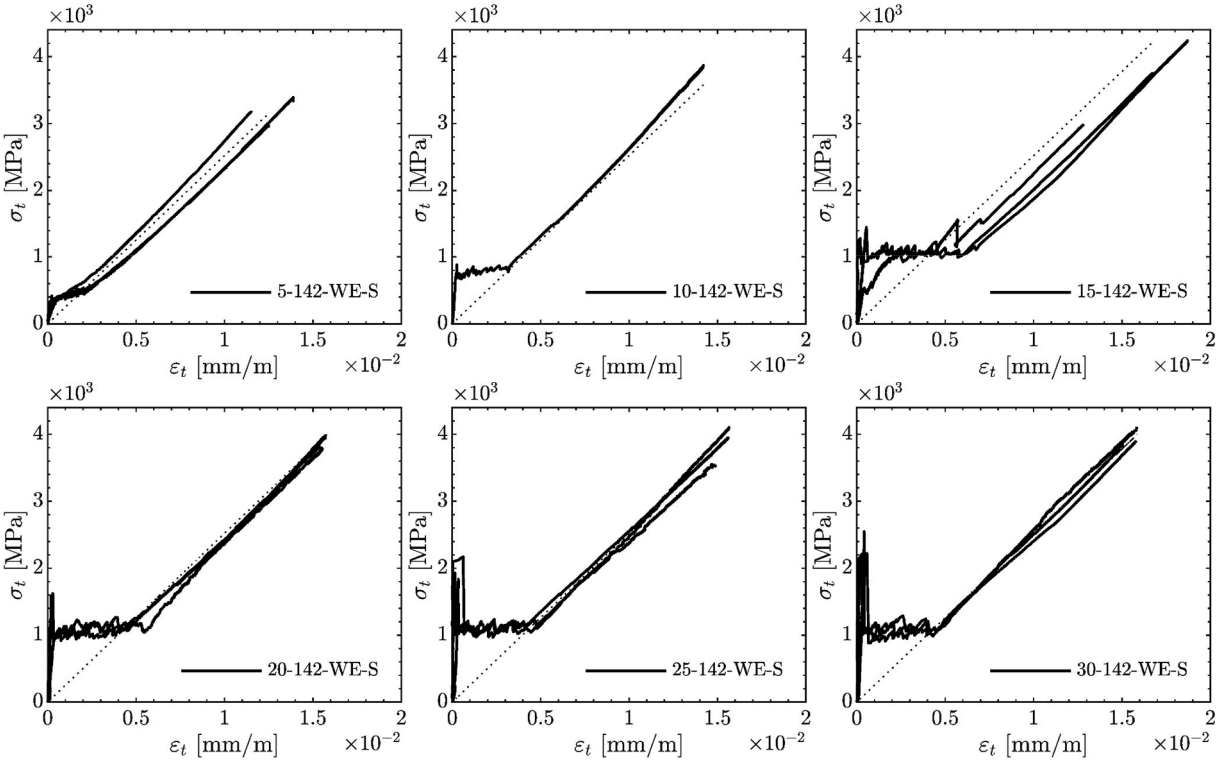

Fig. A5. Stress-Strain Response of Specimens type 142-WE-S.

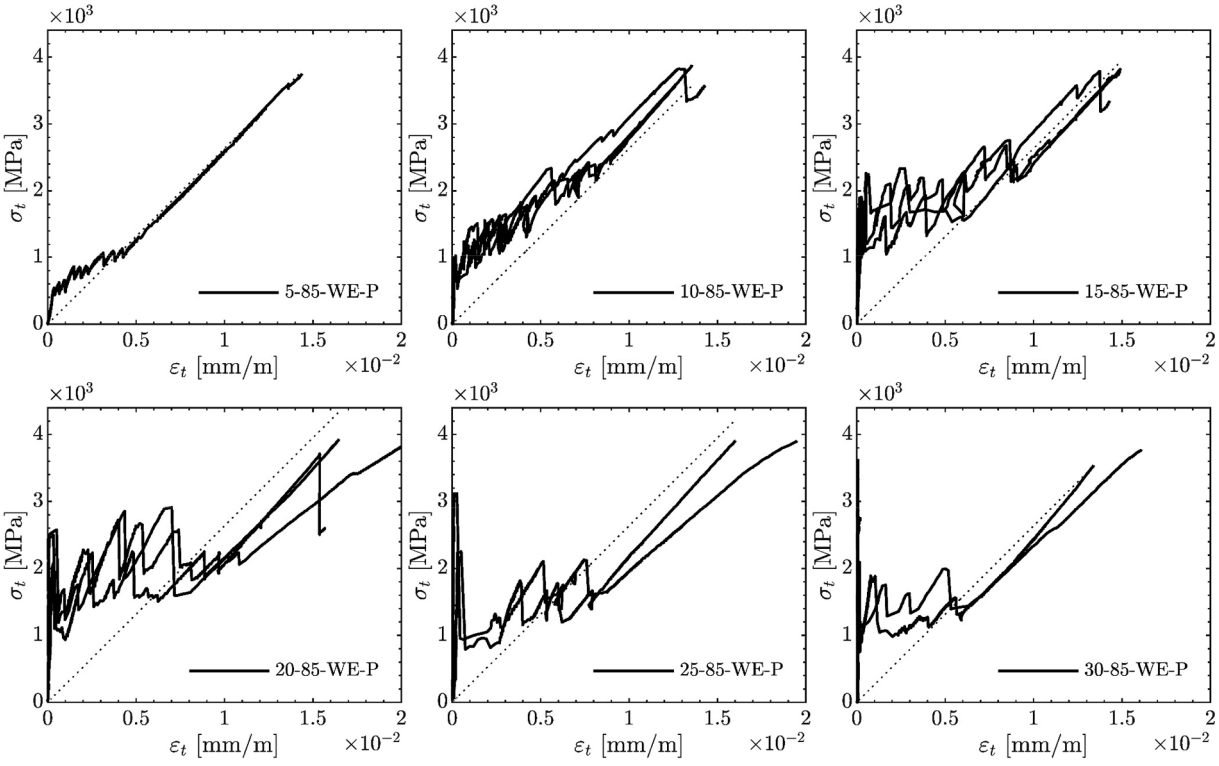

Fig. A6. Stress-Strain Response of Specimens type 85-WE-P.

considers the whole effective depth (see also current provisions in EN 1992–1-1 on the calculation of the crack width). It is also noted here that while efforts are ongoing to establish a model to calculate the splitting tensile stresses and the corresponding resistance of TRC [23,41], ρ_{min} can currently only be determined experimentally for different types of textile reinforcements.

5. Conclusions

This paper presents a comprehensive study on the cracking

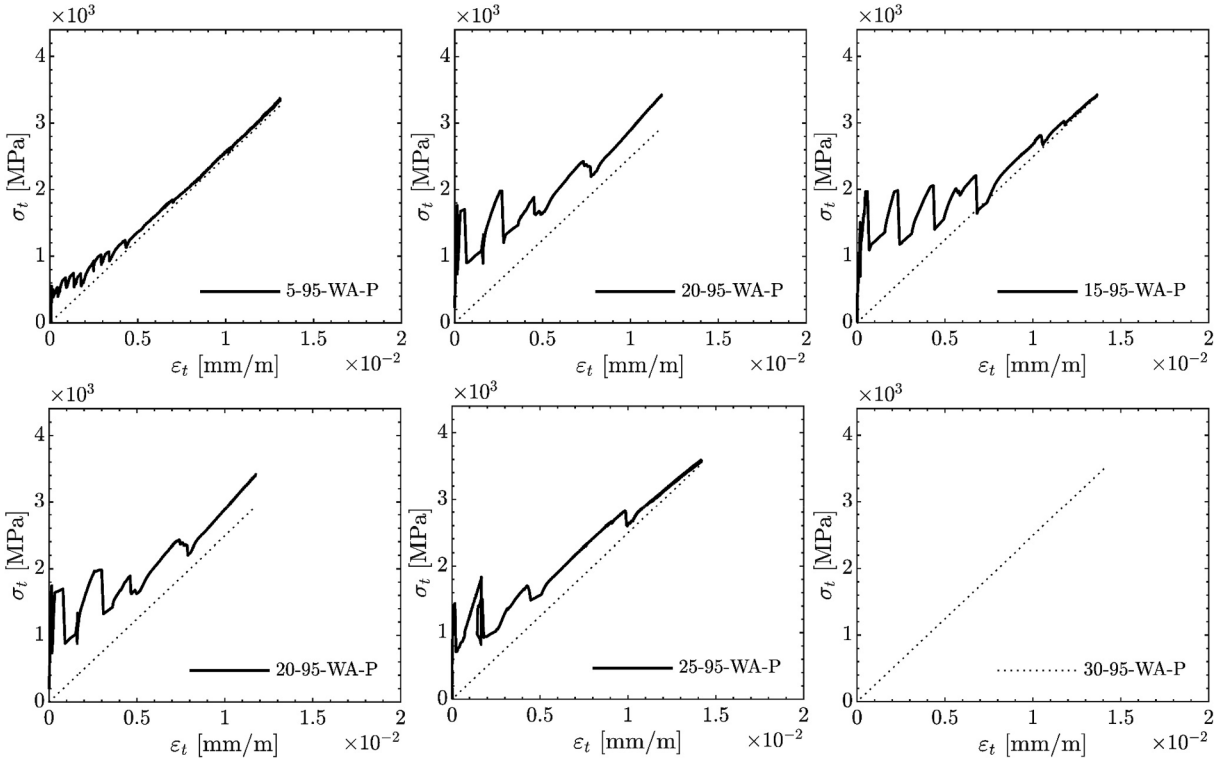

Fig. A7. Stress-Strain Response of Specimens type 95-WA-P.

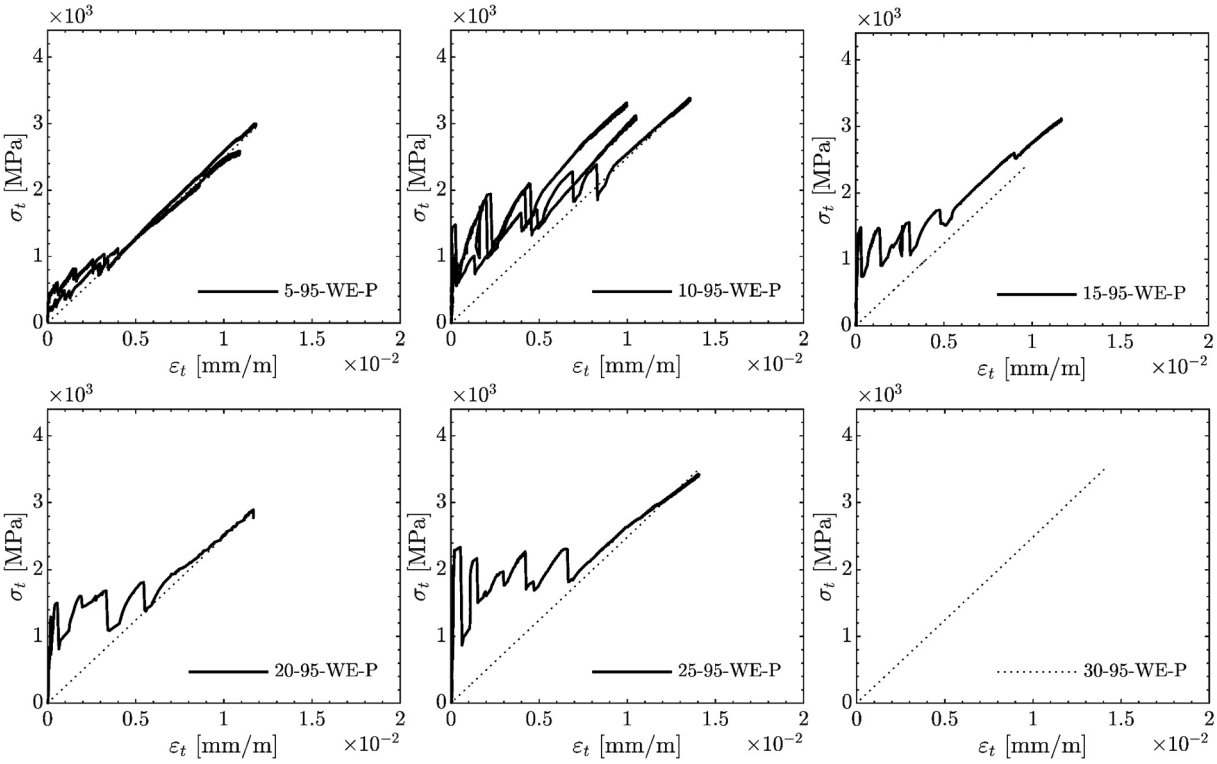

Fig. A8. Stress-Strain Response of Specimens type 95-WE-P.

behaviour of concrete elements reinforced with various epoxy-impregnated heavy tow textiles and subjected to uniaxial tension. The surface finish of the textiles (plain and sand-coated), and the geometry of the fibre strands differed. Concrete covers ranging from 5 mm to 30 mm were used such that the reinforcement ratio also varied. DIC measurements on the front and side of the specimens made it possible to continuously track the cracking process during the uniaxial tensile tests. The following conclusions could be drawn from this study:

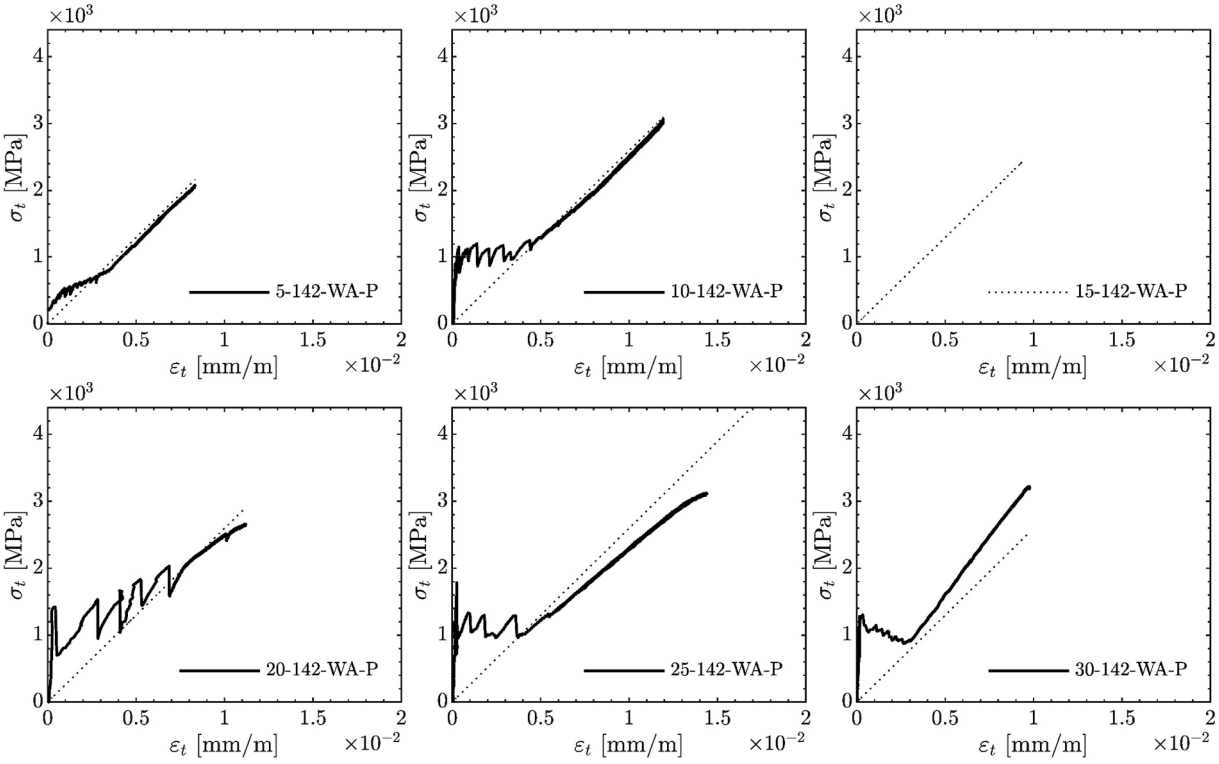

Fig. A9. Stress-Strain Response of Specimens type 142-WA-P.

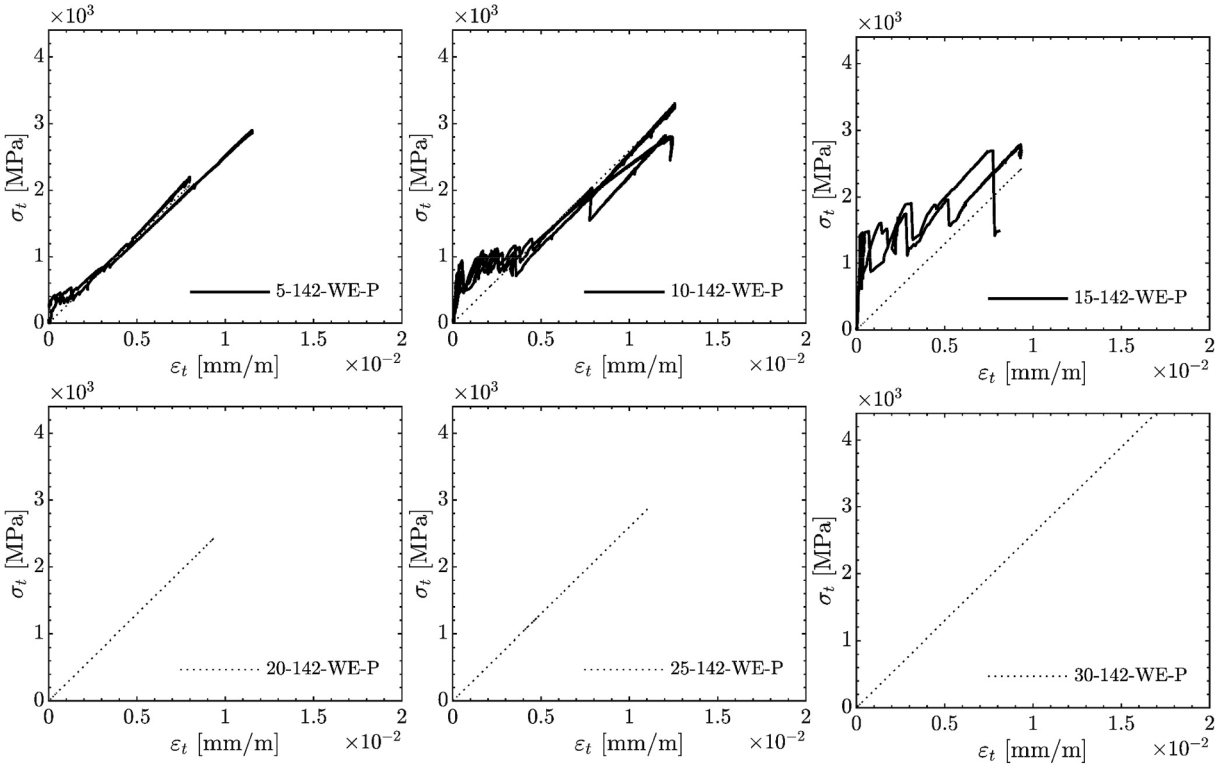

Fig. A10. Stress-Strain Response of Specimens type 142-WE-P.

- In sand-coated textiles, the rough surface created by the sand-coating enables an interlock between the quartz-sand particles and the concrete. This led to relatively small crack spacings and crack widths up to three times smaller compared to specimens with plain textiles. However, the stiff bond behaviour resulted in splitting cracks that initiated at low load levels and subsequently propagated along the reinforcement layer. Although there was no spalling, new transverse cracks only emerged from these splitting cracks.

- In plain textiles, the type of fibre strand binding strongly influences the bond performance since it affects the geometric properties of the fibre strands. It was found that a tricot binding with needle offset is beneficial in the warp direction of plain textiles since it creates a rough surface through a fine pattern of periodic valleys on the fibre strand. This enables an interlocking with the surrounding concrete comparable to that of the sand-coated textiles. The crack width was up to 2.5 times smaller compared to the other plain fibre strands. The knowledge of favourable manufacturing methods and directions allows for a more efficient use of textile reinforcements.
- Due to the progressive splitting crack propagation in the sand-coated specimens, the textile and the concrete separate, thus diminishing any tension stiffening effect. In plain textiles, a tension stiffening was observed. It, however, also gradually decreased at later load stages due to the initiation of splitting cracks. Tension-stiffening effects should therefore not be taken into account for textile-reinforced structures that are prone to splitting cracks in the layer of the textile reinforcement
- The reinforcement ratio strongly affects the occurrence of the splitting cracks. While for larger reinforcement ratios, no such cracks occurred, splitting cracks were observed for reinforcement ratios below a critical ratio ρ_{min}, regardless of the surface finish. This is because smaller crack spacings at higher reinforcement ratios resulted in reduced bond stresses acting between the reinforcement and the concrete. For the textiles described in this paper, ρ_{min} was determined to be 0.26 for Q85 and Q95 and 0.39 for Q142. This refers to a concrete cover thickness of 15 mm in all cases.
- A distinction should be made between the initiation of a splitting crack and concrete cover spalling. Especially in the case of plain textiles, where a slight repeating variation in cross-sectional surface dimensions acts as a wedge, the splitting crack was accompanied by an excessive spalling of the concrete cover. For the sand-coated textiles, however, no such spalling was observed.

CRediT authorship contribution statement

Philipp Preinstorfer: Conceptualization, Methodology, Software, Validation, Formal analysis, Data curation, Writing – original draft, Visualization, Project administration, Funding acquisition. **Serdar Yanik:** Investigation, Validation, Formal analysis, Writing – original draft. **Johannes Kirnbauer:** Conceptualization, Investigation, Data curation, Supervision. **Janet M. Lees:** Supervision, Funding acquisition, Writing – review & editing. **Agathe Robisson:** Supervision, Resources, Writing – review & editing.

Declaration of Competing Interest

The authors declare that they have no known competing financial interests or personal relationships that could have appeared to influence the work reported in this paper.

Data availability

The datasets related to this study are available at the institutional data repository of TU Wien [42] at https://doi.org/10.48436/t1fzp-d2346.

Acknowledgements

This project has received funding from the European Union's Horizon 2020 research and innovation programme under the Marie Sklodowska-Curie grant agreement No 101027058 (https://doi.org/10.3030/101027058).

The authors also express sincere gratitude to Solidian GmbH for their ongoing support in the research on textile-reinforced concrete and to Marco Palma and Anja Fleischhacker for helping with the laser scans.

Appendix

A. Stress-Strain response of all specimens

See the Figs. A1 to A10.

References

[1] Reichenbach S, Preinstorfer P, Hammerl M, Kromoser B. A review on embedded fibre-reinforced polymer reinforcement in structural concrete in Europe. Constr Build Mater 2021;307:124946. https://doi.org/10.1016/j.conbuildmat.2021.124946.
[2] Spelter A, Bergmann S, Bielak J, Hegger J. Long-Term Durability of Carbon-Reinforced Concrete: An Overview and Experimental Investigations. Appl Sci 2019;9:1651. https://doi.org/10.3390/app9081651.
[3] Yilmaz D, Angst U. Korrosionsbedingte Kosten an Ingenieurbauwerken im Schweizer Straßennetz. Beton- Stahlbetonbau 2020;115:448–58. https://doi.org/10.1002/best.202000004.
[4] Stoiber N, Hammerl M, Kromoser B. Cradle-to-gate life cycle assessment of CFRP reinforcement for concrete structures: Calculation basis and exemplary application. J Clean Prod 2021;280:124300. https://doi.org/10.1016/j.jclepro.2020.124300.
[5] Rempel S, Will N, Hegger J, Bielak J. Filigree Textile-Reinforced Concrete Constructions. Proceedings of the Eighth International Conference on Fibre-Reinforced Polymer (FRP) Composites in Civil Engineering (CICE 2016) 2016:525–9.
[6] Santis S, Carozzi FG, Felice G, Poggi C. Test methods for Textile Reinforced Mortar systems. Compos B Eng 2017;127:121–32. https://doi.org/10.1016/j.compositesb.2017.03.016 M4 - Citavi.
[7] Koutas LN, Tetta Z, Bournas DA, Triantafillou TC. Strengthening of Concrete Structures with Textile Reinforced Mortars: State-of-the-Art Review. J Compos Constr 2019;23:03118001. https://doi.org/10.1061/(ASCE)CC.1943-5614.0000882.
[8] Peled A, Mobasher B, Bentur A. Textile Reinforced Concrete. 1st ed. CRC Press; 2017. https://doi.org/10.1201/9781315119151.
[9] Colombo IG, Magri A, Zani G, Colombo M, di Prisco M. Erratum to: Textile Reinforced Concrete: experimental investigation on design parameters. Mater Struct 2013;46:1953–71. https://doi.org/10.1617/s11527-013-0023-7.
[10] Bielak J, Rempel S, Felber M, Durst H, Will N. Rehabilitation of the bridge Rheinsteg near Albbruck with carbon reinforced concrete. Beton- Stahlbetonbau 2021;116:488–97. https://doi.org/10.1002/best.202100024.
[11] Helbig T, Unterer K, Kulas C, Rempel S, Hegger J. Fuß- und Radwegbrücke aus Carbonbeton in Albstadt-Ebingen: Die weltweit erste ausschließlich carbonfaserbewehrte Betonbrücke. Beton- Stahlbetonbau 2016;111:676–85. https://doi.org/10.1002/best.201600058.
[12] Curbach M, Jesse F. Eigenschaften und Anwendung von Textilbeton. Beton-Stahlbetonbau 2009;104:9–16. https://doi.org/10.1002/best.200800653.
[13] El Ghadioui R, Proske T, Tran NL, Graubner C-A. Structural behaviour of CFRP reinforced concrete members under bending and shear loads. Mater Struct 2020;53:63. https://doi.org/10.1617/s11527-020-01496-7.
[14] Botelho Goliath K, T. Cardoso DC, de A. Silva F.. Flexural behavior of carbon-textile-reinforced concrete I-section beams. Compos Struct 2021;260:113540. https://doi.org/10.1016/j.compstruct.2021.113540.
[15] Preinstorfer P, Kromoser B, Kollegger J. Flexural behaviour of filigree slab elements made of carbon reinforced UHPC. Constr Build Mater 2019;199:416–23. https://doi.org/10.1016/j.conbuildmat.2018.12.027.
[16] Preinstorfer P, Huber P, Huber T, Kromoser B, Kollegger J. Experimental investigation and analytical modelling of shear strength of thin walled textile-reinforced UHPC beams. Eng Struct 2021;231:111735. https://doi.org/10.1016/j.engstruct.2020.111735.
[17] Rampini MC, Zani G, Colombo M, di Prisco M. Mechanical Behaviour of TRC Composites: Experimental and Analytical Approaches. Appl Sci 2019;9:1492. https://doi.org/10.3390/app9071492.
[18] Bielak J, Spelter A, Will N, Claßen M. Verankerungsverhalten textiler Bewehrungen in dünnen Betonbauteilen. Beton- Stahlbetonbau 2018;113:515–24. https://doi.org/10.1002/best.201800013.
[19] Preinstorfer P, Kollegger J. New insights into the splitting failure of textile-reinforced concrete. Compos Struct 2020;243:112203. https://doi.org/10.1016/j.compstruct.2020.112203.
[20] Schütze E, Curbach M. Zur experimentellen Charakterisierung des Verbundverhaltens von Carbonbeton mit Spalten als maßgeblichem Versagensmechanismus/Experimental characterisation of the bond behaviour of carbon reinforced concrete with concrete splitting as significant failure mode. Bauingenieur 2019;94:133–41. https://doi.org/10.37544/0005-6650-2019-04-61.
[21] Bielak J, Schöneberg J, Classen M, Hegger J. Shear capacity of continuous concrete slabs with CFRP reinforcement. Constr Build Mater 2022;320:126117. https://doi.org/10.1016/j.conbuildmat.2021.126117.

[22] Preinstorfer P. Zur Spaltrissbildung von textilbewehrtem Beton. TU Wien Academic Press; 2020.
[23] Preinstorfer P, Kromoser B. Influence of geometrical parameters on the splitting forces in textile-reinforced concrete. Mater Struct 2020;53:152. https://doi.org/10.1617/s11527-020-01590-w.
[24] Morales Cruz C, Raupach M. Influence of the surface modification by sanding of carbon textile reinforcements on the bond and load-bearing behavior of textile reinforced concrete. MATEC Web Conf 2019;289:04006. https://doi.org/10.1051/matecconf/201928904006.
[25] Preinstorfer P, Kromoser B, Kollegger J. Einflussparameter auf die Spaltrissbildung in Textilbeton. Beton- Stahlbetonbau 2018;113:877–85. https://doi.org/10.1002/best.201800071.
[26] Hammerl M, Stoiber N, Hämmerle J, Shams A, Bischoff T, Kromoser B. Verbundverhalten umwickelter CFK-Stäbe in Beton – Kurzzeituntersuchung der Verbundeigenschaften mittels Pull-out-Tests. Beton- Stahlbetonbau 2021;116:935–46. https://doi.org/10.1002/best.202100079.
[27] Schütze E, Bielak J, Scheerer S, Hegger J, Curbach M. Einaxialer Zugversuch für Carbonbeton mit textiler Bewehrung. Beton- Stahlbetonbau 2018;113:33–47. https://doi.org/10.1002/best.201700074.
[28] Valeri P, Fernàndez Ruiz M, Muttoni A. Tensile response of textile reinforced concrete. Constr Build Mater 2020;258:119517. https://doi.org/10.1016/j.conbuildmat.2020.119517.
[29] Hartig J, Jesse F, Schicktanz K, Häußler-Combe U. Influence of experimental setups on the apparent uniaxial tensile load-bearing capacity of Textile Reinforced Concrete specimens. Mater Struct 2012;45:433–46. https://doi.org/10.1617/s11527-011-9775-0.
[30] Yanik S. Einfluss der Überdeckung auf die Rissbildung von Hochleistungsbeton mit Carbonbewehrung unter Zugbeanspruchung. Vienna University of Technology; 2021.
[31] Correlate G. Brunswick. Germany: Carl Zeiss GOM Metrology GmbH; 2019.
[32] Rempel S, Ricker M, Feiri T. Stochastic approach for the material properties of reinforcing textiles for the design of concrete members. Sci Rep 2021;11:21976. https://doi.org/10.1038/s41598-021-01032-9.
[33] Huber P, Huber T, Kollegger J. Investigation of the shear behavior of RC beams on the basis of measured crack kinematics. Eng Struct 2016;113:41–58. https://doi.org/10.1016/j.engstruct.2016.01.025.
[34] Gehri N, Mata-Falcón J, Kaufmann W. Automated crack detection and measurement based on digital image correlation. Constr Build Mater 2020;256:119383. https://doi.org/10.1016/j.conbuildmat.2020.119383.
[35] Vořechovský M, Li Y, Rypl R, Chudoba R. Tensile behavior of carbon textile concrete composite captured using a probabilistic multiscale multiple cracking model. Compos Struct 2021;277:114624. https://doi.org/10.1016/j.compstruct.2021.114624.
[36] Yao Y, Silva FA, Butler M, Mechtcherine V, Mobasher B. Tension stiffening in textile-reinforced concrete under high speed tensile loads. Cem Concr Compos 2015;64:49–61. https://doi.org/10.1016/j.cemconcomp.2015.07.009.
[37] Preinstorfer P, Yanik S, Kirnbauer J, Robisson A. Investigations into the Cracking behaviour of Epoxy-Impregnated textile-reinforced concrete, Oslo: 2022.
[38] Aci 440.1r-15.. Guide for the Design and Construction of Structural Concrete Reinforced with Fiber-Reinforced Polymer Bars. Michigan, United States: American Concrete Institute; 2015.
[39] Fleischhacker A. Untersuchungen zum Einfluss unterschiedlicher Oberflächenbeschaffenheiten auf das Verbundverhalten von Textilbeton. Vienna University of Technology; 2022.
[40] Preinstorfer P, Lees J. Modelling of the splitting failure mode in textile-reinforced concrete. Fibre Polymer Composites in Construction, Bradford, UK: 2022, p. 1–5.
[41] Beßling M, Orlowsky J. Quantification of the Influence of Concrete Width per Fiber Strand on the Splitting Crack Failure of Textile Reinforced Concrete (TRC). Polymers 2022;14:489. https://doi.org/10.3390/polym14030489.
[42] Preinstorfer P. Data supporting: Cracking behaviour of textile-reinforced concrete with varying concrete cover and textile surface finish (1.0.0) [Data set]. Wien: TU; 2023. https://doi.org/10.48436/t1fzp-d2346.